Form factors for the processes $B_c^+ \to D^0 \ell^+ \nu_\ell$ and $B_c^+ \to D_s^+ \ell^+ \ell^- (\nu\bar{\nu})$ from lattice QCD

Laurence J. Cooper[1,2,*] Christine T. H. Davies,[1,†] and Matthew Wingate[2,‡]

(HPQCD Collaboration)

[1]*SUPA, School of Physics and Astronomy, University of Glasgow, Glasgow, G12 8QQ, United Kingdom*
[2]*Department of Applied Mathematics and Theoretical Physics, University of Cambridge,
Cambridge, CB3 0WA, United Kingdom*

We present results of the first lattice QCD calculations of the weak matrix elements for the decays $B_c^+ \to D^0 \ell^+ \nu_\ell$, $B_c^+ \to D_s^+ \ell^+ \ell^-$ and $B_c^+ \to D_s^+ \nu\bar{\nu}$. Form factors across the entire physical q^2 range are then extracted and extrapolated to the continuum limit with physical quark masses. Results are derived from correlation functions computed on MILC Collaboration gauge configurations with three different lattice spacings and including $2 + 1 + 1$ flavors of sea quarks in the highly improved staggered quark (HISQ) formalism. HISQ is also used for all of the valence quarks. The uncertainty on the decay widths from our form factors for $B_c^+ \to D^0 \ell^+ \nu_\ell$ is similar in size to that from the present value for V_{ub}. We obtain the ratio $\Gamma(B_c^+ \to D^0 \mu^+ \nu_\mu)/|\eta_{\mathrm{EW}} V_{ub}|^2 = 4.43(63) \times 10^{12} \text{ s}^{-1}$. Combining our form factors with those found previously by HPQCD for $B_c^+ \to J/\psi \mu^+ \nu_\mu$, we find $|V_{cb}/V_{ub}|^2 \Gamma(B_c^+ \to D^0 \mu^+ \nu_\mu)/\Gamma(B_c^+ \to J/\psi \mu^+ \nu_\mu) = 0.257(36)_{B_c \to D}(18)_{B_c \to J/\psi}$. We calculate the differential decay widths of $B_c^+ \to D_s^+ \ell^+ \ell^-$ across the full q^2 range and give integrated results in q^2 bins that avoid possible effects from charmonium and $u\bar{u}$ resonances. For example, we find that the ratio of differential branching fractions integrated over the range $q^2 = 1 \text{ GeV}^2$–6 GeV^2 for $B_c^+ \to D_s^+ \mu^+ \mu^-$ and $B_c^+ \to J/\psi \mu^+ \nu_\mu$ is $6.31(90)_{B_c \to D_s}(65)_{B_c \to J/\psi} \times 10^{-6}$. We also give results for the branching fraction of $B_c^+ \to D_s^+ \nu\bar{\nu}$. Prospects for reducing our errors in the future are discussed.

I. INTRODUCTION

In this paper, we use lattice QCD methods to calculate the form factors that capture the nonperturbative physics of the pseudoscalar B_c^+ meson decaying weakly into either $D^0 \ell^+ \nu_\ell$, $D_s^+ \ell^+ \ell^-$ or $D_s^+ \nu\bar{\nu}$. This is the first time that these calculations have been performed. To ascertain the successes and shortcomings of the Standard Model's description of the physics observed in experiment, it is essential to produce predictions from the Standard Model at high precision that fully incorporate the nonperturbative strong interaction phenomenology of hadrons. Lattice QCD

provides a route towards achieving this for the weak matrix elements studied here.

We present the first lattice QCD calculation of the form factors f_0 and f_+ for the vector current matrix elements for $B_c^+ \to D^0 \ell^+ \nu_\ell$ throughout the entire range of physical momentum transfer squared, q^2. An accurate prediction from the Standard Model of the normalization and shape of the form factors for $B_c^+ \to D^0 \ell^+ \nu_\ell$ will complement observations of this process from experiment and ultimately lead to a new exclusive determination of the CKM matrix element $|V_{ub}|$ in the future. LHCb expects [1] that Upgrade II will make it possible to have a measurement of $B_c^+ \to D^0 \mu^+ \nu_\mu$ with sufficient accuracy to offer a competitive determination of V_{ub}. Further scrutiny of V_{ub} is needed to address the long-standing unresolved tension between inclusive and exclusive determinations (for example, see world averages of V_{ub} from both inclusive and exclusive determinations in [2]). Exclusive determinations of V_{ub} using form factors from lattice QCD have so far been focused on the semileptonic decays $B \to \pi$, $B_s \to K$ and $\Lambda_b \to p$, so determining V_{ub} via semileptonic $B_c \to D$ will offer another data point. We also consider the branching

[*]Laurence.Cooper@glasgow.ac.uk
[†]Christine.Davies@glasgow.ac.uk
[‡]M.Wingate@damtp.cam.ac.uk

fraction ratio of $B_c \to D$ and, using form factors from [3], the process $B_c \to J/\psi$. This allows the combination V_{ub}/V_{cb} to be examined given experimental information on this ratio.

Alongside our calculation of the form factors for $B_c^+ \to D^0 \ell^+ \nu_\ell$, we also carry out a lattice QCD calculation of the form factors f_0, f_+ and f_T for the vector and tensor current matrix elements of the rare processes $B_c^+ \to D_s^+ \ell^+ \ell^-$ and $B_c^+ \to D_s^+ \nu \bar{\nu}$. These semileptonic decays are examples of flavor-changing, neutral current (FCNC) processes, and they are of interest in their own right. Such processes are not allowed at tree level in the Standard Model; thus, contributions from physics beyond the Standard Model may be more visible than with tree-level decays. Therefore, FCNC transitions are an important avenue towards understanding the validity of the Standard Model.

The form factors calculated here are part of an ongoing program by HPQCD to study weak decays of mesons containing a bottom quark. Our ultimate aim is to determine Standard Model contributions at high enough precision such that comparison with experiment reveals or constrains new physics scenarios. We are now in an era in which fully relativistic lattice QCD calculations of decays of mesons containing bottom quarks are achievable. We use the highly improved staggered quark formalism (HISQ) [4], which is specifically designed to have small discretization errors. The large mass of the b quark requires very fine lattices to control discretization effects. We simulate with bottom quarks at their physical mass on our finest lattice and unphysically light bottom quarks on the coarser lattices. Together this data inform the limit of vanishing lattice spacing and physical quark masses through HPQCD's "heavy-HISQ" strategy. Recent calculations that have established the method for determining semileptonic form factors include [3,5–9].

We also investigate strategies for improving on this first calculation of the form factors for $B_c \to D$ and $B_c \to D_s$. These methods will inform the strategy for other future calculations of heavy-to-light quark decays. Form factors with smaller uncertainties will offer a more powerful examination of the precision flavor physics we envisage. To minimize cost, we try these improvements in the $B_c \to D_s$ case only.

The sections in this paper are organized as follows:

(i) Section II gives a comprehensive description of how the form factors across the entire physical range of 4-momentum transfer are obtained from lattice correlation functions. Results from fitting the correlation functions are attached to this paper [10]. Appendix A discusses intermediate results from the correlation function fitting and form factor fits.

(ii) In Sec. III, we present our form factors obtained from taking the physical-continuum limit of the lattice data. We plot and tabulate observables found from combining our form factors with CKM matrix elements and known Wilson coefficients. Details of the form factor fits are presented in Appendix B. Appendix C gives the means for the reader to reconstruct our form factors.

(iii) In Sec. IV, we investigate extensions to our calculations that aim to improve the precision of our determination of the physical-continuum form factors in a future update. These discussions will guide other calculations of heavy-to-light decay processes in the future.

II. CALCULATION DETAILS

A. Form factors

Our calculations use equal-mass u and d quarks. The corresponding quark flavor is denoted as l. In this paper, we use the shorthand $B_c \to D_l$ and $B_c \to D_s$ to label the two different decays considered here. The subscript on the D_l and D_s mesons denotes the flavor of the daughter quark that arises from the decay of the parent b quark.

The form factors f_0 and f_+ are defined through the vector current matrix element

$$\langle D_{l(s)}(\boldsymbol{p}_2)|V^\mu|B_c(\boldsymbol{p}_1)\rangle$$
$$= f_0^{l(s)}(q^2)\left[\frac{M_{B_c}^2 - M_{D_{l(s)}}^2}{q^2}q^\mu\right]$$
$$+ f_+^{l(s)}(q^2)\left[p_2^\mu + p_1^\mu - \frac{M_{B_c}^2 - M_{D_{l(s)}}^2}{q^2}q^\mu\right] \quad (1)$$

where $q = p_1 - p_2$ is the 4-momentum transfer, and, since we study the transitions $B_c \to D_l$ and $B_c \to D_s$ in tandem throughout this article, we will use the notation $f_{0,+}^l$ and $f_{0,+,T}^s$, respectively, to differentiate between their form factors.

The semileptonic weak decay $B_c^+ \to D^0 \ell^+ \nu_\ell$ is facilitated by a $b \to uW^-$ quark transition. Ignoring isospin breaking effects and possible long-distance QED corrections, the differential decay rate is related to the form factors through

$$\frac{d\Gamma}{dq^2} = \eta_{\mathrm{EW}}^2 |V_{ub}|^2 \frac{G_F^2}{24\pi^3}\left(1 - \frac{m_\ell^2}{q^2}\right)^2 |\boldsymbol{q}|$$
$$\times \left[\left(1 + \frac{m_\ell^2}{2q^2}\right)|\boldsymbol{q}|^2 f_+^l(q^2)^2\right.$$
$$\left. + \frac{3m_\ell^2}{8q^2}\frac{(M_{B_c}^2 - M_D^2)^2}{M_{B_c}^2}f_0^l(q^2)^2\right]. \quad (2)$$

This is proportional to $\eta_{\mathrm{EW}}^2 |V_{ub}|^2$, where the factor $\eta_{\mathrm{EW}} = 1.0062(16)$ is the electroweak correction to G_F [11] and we use the same value as in [3] for $B_c^+ \to J/\psi\ell^+\nu_\ell$. The mass of the lepton in the final state is m_ℓ. The contribution of f_0 is suppressed by the lepton mass and so is only relevant for

TABLE I. Parameters for the MILC ensembles of gluon field configurations. The lattice spacing a is determined from the Wilson flow parameter w_0 [19]. The physical value $w_0 = 0.1715(9)$ fm was fixed from f_π in [20]. Sets 1 and 2 have $a \approx 0.09$ fm. Set 3 has $a \approx 0.059$ fm, and set 4 has $a \approx 0.044$ fm. Sets 1, 3, and 4 have unphysically massive light quarks such that $m_l/m_s = 0.2$. We give $M_\pi L$ and M_π values for each lattice in the fifth and sixth columns [24]. In the seventh column, we give n_{cfg}, the number of configurations used for each set. We also use four different positions for the source on each configuration to increase statistics.

Set	Handle	w_0/a	$N_x^3 \times N_t$	$M_\pi L$	M_π MeV	n_{cfg}	am_l^{sea}	am_s^{sea}	am_c^{sea}	am_l^{val}	am_s^{val}	am_c^{val}	T
1	Fine	1.9006(20)	$32^3 \times 96$	4.5	316	500	0.0074	0.037	0.440	0.0074	0.0376	0.450	14, 17, 20
2	Fine-physical	1.9518(17)	$64^3 \times 96$	3.7	129	500	0.00120	0.0364	0.432	0.00120	0.036	0.433	14, 17, 20
3	Superfine	2.896(6)	$48^3 \times 144$	4.5	329	250	0.0048	0.024	0.286	0.0048	0.0245	0.274	22, 25, 28
4	Ultrafine	3.892(12)	$64^3 \times 192$	4.3	315	250	0.00316	0.0158	0.188	0.00316	0.0165	0.194	31, 36, 41

the decay mode $B_c^+ \to D^0\tau^+\nu_\tau$. The physical range of momentum transfer

$$m_\ell^2 < q^2 < (M_{B_c} - M_D)^2 = 19.4 \text{ GeV}^2 \qquad (3)$$

is large here because of the large mass of the b quark.

The short-distance physics of the FCNC transition $B_c \to D_s$ is described by form factors $f_{0,+}$ of the vector current $\bar{s}\gamma^\mu b$ and the form factor f_T of the tensor operator $T^{\mu\nu} = \bar{s}\sigma^{\mu\nu}b$ where $2\sigma^{\mu\nu} = [\gamma^\mu, \gamma^\nu]$. The form factor f_T is defined through the matrix element of the tensor operator

$$\langle D_s(\boldsymbol{p}_2)|T^{k0}|B_c(\boldsymbol{p}_1)\rangle = \frac{2iM_{B_c}p_2^k}{M_{B_c} + M_{D_s}}f_T^s(m_b; q^2). \quad (4)$$

The tensor form factor f_T^s is scheme and scale dependent. We will quote results in the $\overline{\mathrm{MS}}$ scheme at scale 4.8 GeV. Within the Standard Model, the tensor form factor f_T is relevant for the rare decay $B_c^+ \to D_s^+\ell^+\ell^-$ that proceeds via $b \to s$, but not for $B_c^+ \to D_s^+\nu\bar{\nu}$ or the tree-level decay $B_c^+ \to D^0\ell^+\nu_\ell$. The daughter quark for $B_c \to D_s$ is heavier than in the case of $B_c \to D$. The computational expense of computing lattice quark propagators increases as the quark mass decreases, so computing the form factors for $B_c \to D_s$ amounts to a less expensive computation than for $B_c \to D$. Hence, we compute the tensor form factor f_T only for the process $B_c \to D_s$. In the future, we intend to also calculate the tensor form factor for $b \to d$ processes.

From matrix elements of the scalar density and vector current on four different lattices with a selection of heavy and light quark masses, we fit the corresponding form factor data to obtain the form factors in the continuum limit with physical quark masses. By combining existing values of CKM matrix elements V_{ts} and V_{tb}, along with values of Wilson coefficients, we predict the decay rate for $B_c^+ \to D_s^+\ell^+\ell^-$ within the scope of Standard Model phenomenology. The expression for the decay rate follows similarly to Sec. VII in [12] for $B \to K\ell^+\ell^-$ where we take the $\overline{\mathrm{MS}}$ scale to be m_b for the tensor form factor. We also predict the decay rate for $B_c^+ \to D_s^+\nu\bar{\nu}$ using an expression similar to that for $B \to K\nu\bar{\nu}$ in [13,14].

B. Ensembles and parameters

We use ensembles with $2 + 1 + 1$ flavors of HISQ sea quarks generated by the MILC Collaboration [15–17]. Table I presents details of the ensembles. The Symanzik-improved gluon action used is that from [18], where the gluon action is improved perturbatively through $\mathcal{O}(\alpha_s a^2)$, including the effect of dynamical HISQ sea quarks. The lattice spacing is identified by comparing the physical value for the Wilson flow parameter [19] $w_0 = 0.1715(9)$ fm [20] with lattice values for w_0/a from [21,22]. The following calculations feature strange quarks at their physical mass and equal-mass up and down quarks, with mass denoted by m_l. We use lattices with $m_s/m_l = 5$ in the sea and also the physical value $m_s/m_l = 27.4$ [23]. The corresponding pion masses are tabulated in Table I [24]. Values for $M_\pi L$ (where $L = aN_x$) are also given in Table I as an indicator of sensitivity to finite-volume effects. In the more precise calculation of [12] for the form factors for $B \to K$, finite-volume effects were found to be small compared to final uncertainties. Hence, we expect finite-volume effects to be very small compared to the uncertainties we achieve in this first calculation, so we ignore them. The valence strange and charm quark masses used here, also tabulated in Table I, were tuned in [22,25] slightly away from the sea quark masses to yield results that more closely correspond to physical values. Corrections due to the tuning of valence strange quark and charm quark masses away from the masses of the sea quarks should, at leading order, simply amount to a correction linear in the sea mass mistuning, which we allow for in our fit of the form factors (described in Sec. II F). We take the mass of valence l quarks to be equal to the mass of the sea l quarks. We ignore isospin-breaking and QED effects in this first calculation. The propagators were calculated using the MILC code [26].

The numerical challenge of generating the finest lattices that we use here means that the ensembles do not fully explore the space of all possible topological charges. The effects of topology freezing on meson phenomenology calculated on these lattices were explored in [27]. It was found that a topological adjustment of 1% is required for the D meson decay constant on the ultrafine lattice (set 4).
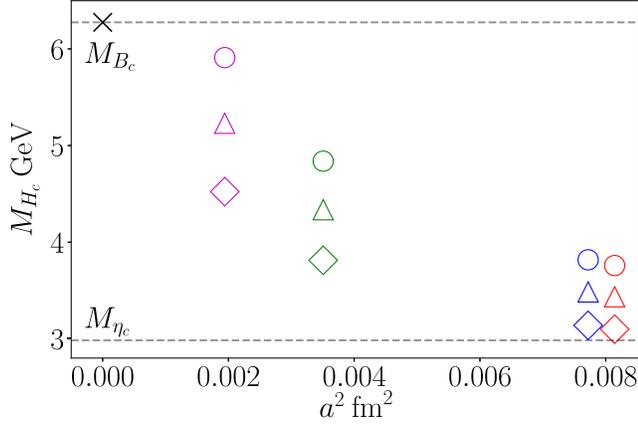
FIG. 1. The mass M_{H_c} of the heavy-charm pseudoscalar meson is plotted against the lattice spacing squared for each of the values $am_h = 0.5, 0.65, 0.8$ used in the heavy-HISQ calculation. Values for M_{H_c} are obtained from fitting the correlation functions as described in Sec. II E. The continuum-physical point is denoted by a cross at $a = 0$ fm and $M_{H_c} = M_{B_c}$ from experiment [28]. Data from sets 1–4 are denoted by the colors red, blue, green and magenta, respectively. Data for $am_h = 0.5, 0.65, 0.8$ can be identified by the diamond, triangle and circle markers, respectively. These choices will be repeated in all subsequent plots.

The adjustment for D_s is negligible, and this is also expected to be the case for the B_c meson. The sizes of the errors achieved in our calculations here are such that effects from topological freezing (which could be of similar size for form factors as those seen for decay constants) are negligible, so we ignore them. In the future, more accurate form factor calculations may need to incorporate adjustments due to nonequilibrated topological charge distributions on the ultrafine and finer lattices.

The heavy-HISQ method sees all flavors of quarks implemented with the HISQ [4] formalism. This is a fully relativistic approach which involves calculations for a set of quark masses on ensembles of lattices with a range of fine lattice spacings, enabling a fit from which the physical result at the b quark mass in the continuum can be determined. In our heavy-HISQ method, we utilize a valence HISQ quark with mass m_h that takes values between m_c and m_b. We describe this quark as "heavy." In the limit of physical quark masses, the heavy quark will coincide with the b quark. Regarding the mesons that this

quark forms with a constituent charm, strange or light quark, we adopt nomenclature for these mesons that is similar to mesons with a constituent bottom quark. For example, we label the low-lying heavy-charm pseudoscalar meson as H_c. If we were to take $m_h = m_b$, then this meson would coincide with the B_c pseudoscalar meson.

This heavy-HISQ calculation uses bare heavy quark masses $am_h = 0.5, 0.65, 0.8$ on all four sets in Table I. The masses of the corresponding heavy-charm pseudoscalar mesons H_c are plotted in Fig. 1. The mass of the heaviest heavy-charm pseudoscalar meson is only 6% lighter than the physical B_c meson.

Momentum is inserted only into the valence light (strange) quark of the $D_{l(s)}$ meson; thus, the initial H_c meson is always at rest on the lattice. The momentum insertion is implemented through partially twisted boundary conditions [29,30] in the $(1 \quad 1 \quad 1)$ direction. The twists used on each set are given in Table II. The twist angle θ is related to the three-momentum transfer $\boldsymbol{q} = \boldsymbol{p}_1 - \boldsymbol{p}_2$ by

$$|\boldsymbol{q}| = \frac{\pi\theta\sqrt{3}}{aN_x}. \tag{5}$$

For example, zero twist ($\theta = 0$) corresponds to zero recoil where q^2 takes its maximum physical value, which we denote as $q^2_{\max}$. In previous studies, such as Fig. 3 in [6], it has been observed that the continuum dispersion relation is closely followed for mesons with staggered quarks, particularly on the finer lattices. The twists we use allow a considerable proportion of the physical q^2 range to be probed. Most of the twists in Table II originate from a variety of past calculations in which the corresponding propagators were saved for future use.

Figure 2 shows the q^2 realized by the twists in Table II. The values of $q^2/q^2_{\max}$ are given for each twist and heavy quark mass for both $H_c \to D_l$ and $H_c \to D_s$. Twists that give negative q^2 are unphysical but will nevertheless aid the fits of the form factors across the physical range. For all of the sets except one, all of the q^2 range is covered for the lightest heavy quark mass value $am_h = 0.5$ (recall that Fig. 1 shows the corresponding mass of the heavy-charm pseudoscalar mesons). For the finest lattice, set 4 in Table I, Fig. 2 shows for the largest heavy quark mass, close to m_b.

TABLE II. Twists used for heavy-HISQ calculations on each of the four sets given in Table I. The twists are in the $(1 \quad 1 \quad 1)$ direction and defined in Eq. (5). The corresponding values of q^2 as a proportion of $q^2_{\max}$ are shown in Fig. 2.

Set	twists θ for $B_c \to D_s$	Twists θ for $B_c \to D_l$
1	0, 0.4281, 1.282, 2.141, 2.570	0, 0.4281, 1.282, 2.141, 2.570
2	0, 0.8563, 2.998, 5.140	0, 3.000, 5.311
3	0, 1.261, 2.108, 3.624, 4.146	0, 1.261, 2.108, 2.666
4	0, 0.706, 1.529, 2.235, 4.705	0, 0.706, 1.529, 2.235, 4.705
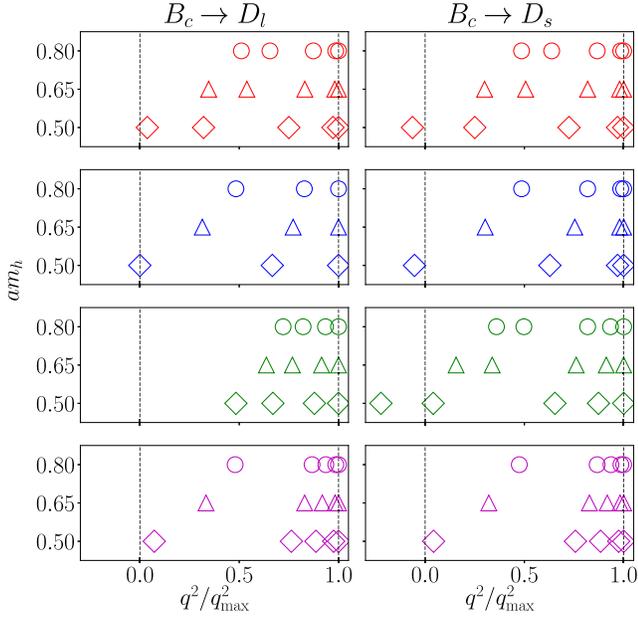
FIG. 2. The q^2 values on each set as a proportion of the maximum value $q_{\max}^2 = (M_{H_c} - M_{D_{l(s)}})^2$. From top to bottom, data from sets 1–4 are displayed (see Table I). For different am_h on a given set, the same twists were used. As described in the caption for Fig. 1, data from sets 1–4 and heavy quark masses am_h are denoted by different colors and marker styles. Values used here for the masses of the initial and final mesons are found from fits of correlation functions (to be discussed in Sec. II E).

C. Extracting form factors from matrix elements

The conserved HISQ vector current is given explicitly in Appendix A of [31]. It takes the form of a complicated linear combination of multilink point-split operators. While the conserved current has the advantage that it does not require a multiplicative renormalization factor, its form is unwieldy for lattice computations. Hence, we elect to use simple local currents that are not conserved and determine the corresponding renormalizations.

Our calculation uses HISQ quarks exclusively. In particular, since we use HISQ for both the parent heavy quark and the daughter light or strange quark, we can use the partially conserved vector current Ward identity to relate matrix elements of the renormalized local vector current $Z_V V_{\text{local}}^\mu$ with matrix elements of the local scalar density through

$$q_\mu \langle D_{l(s)} | V_{\text{local}}^\mu | H_c \rangle Z_V = (m_h - m_{l(s)}) \langle D_{l(s)} | S_{\text{local}} | H_c \rangle. \quad (6)$$

This holds since the mass and scalar density multiplicative renormalization factors Z_m and Z_S satisfy $Z_m Z_S = 1$. Using Eq. (6) to determine Z_V is a fully nonperturbative strategy. Up to discretization effects, the renormalization factor is independent of q^2, so it is sufficient to deduce its value at zero recoil ($\boldsymbol{q} = \boldsymbol{0}$ and maximum q^2). Using different staggered "tastes" of mesons in Eq. (6) will contribute a

discretization error that is accounted for when fitting the lattice form factor data. At zero recoil, Eq. (6) only features matrix elements of the scalar density and the *temporal* component of the vector current, so we do not compute matrix elements of the *spatial* components of the vector current (though they will be considered in Sec. IV B as part of our investigation towards future improvements).

Combining Eqs. (6) and (1) yields

$$f_0^{l(s)}(q^2) = \langle D_{l(s)} | S_{\text{local}} | H_c \rangle \frac{m_h - m_{l(s)}}{M_{H_c}^2 - M_{D_{l(s)}}^2}. \quad (7)$$

We use Eq. (7) to extract f_0 from the given combination of quark masses, meson masses and the matrix element of the scalar density.

Equation (1) for $\mu = 0$ can be trivially rearranged to yield

$$f_+^{l(s)}(q^2) = \frac{Z_V \langle D_{l(s)} | V_{\text{local}}^0 | H_c \rangle - q^0 f_0^{l(s)}(q^2) \frac{M_{H_c}^2 - M_{D_{l(s)}}^2}{q^2}}{p_2^0 + p_1^0 - q^0 \frac{M_{H_c}^2 - M_{D_{l(s)}}^2}{q^2}}. \quad (8)$$

At zero recoil, the denominator vanishes so f_+ cannot be extracted here. In practice, using Eq. (8) near zero recoil is problematic since both the numerator and denominator approach 0 as q^2 increases towards its maximum value at zero recoil. This is discussed further in Appendix B. [In Sec. IV B, we consider an alternative extraction of f_+ by using Eq. (1) with $\mu \neq 0$.]

Finally, the tensor form factor is obtained through

$$f_T^s(q^2) = \frac{Z_T \langle D_s | T_{\text{local}}^{1,0} | H_c \rangle (M_{H_c} + M_{D_s})}{2i M_{H_c} p_2^1}, \quad (9)$$

where $T_{\text{local}}^{1,0}$ is the local tensor operator and Z_T is its multiplicative renormalization factor that takes the lattice tensor current to the $\overline{\text{MS}}$ scheme. We use values of the associated multiplicative renormalization factor Z_T obtained using the RI-SMOM intermediate scheme. We give these values in Table III. Values in the RI-SMOM scheme at scale 3 GeV are converted to scale 4.8 GeV in the

TABLE III. Values used for the multiplicative renormalization factor Z_T of the tensor operator obtained from Tables VIII and IX in [32] at scale m_b in the $\overline{\text{MS}}$ scheme. The set handles correspond to those given in Table I. The top row gives the mean values of Z_T, and the rows beneath give the covariance matrix scaled by a factor of 10^5.

Sets 1 and 2	Set 3	Set 4
0.9980	1.0298	1.0456
0.6250	0.6242	0.6059
	0.6250	0.6057
		0.6250
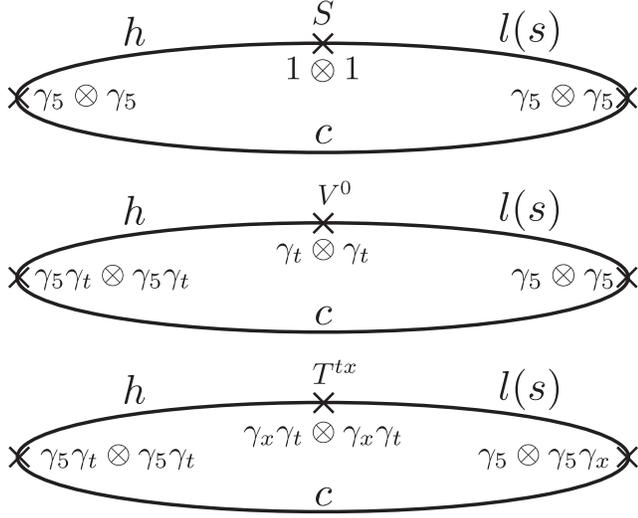
FIG. 3. Diagrammatic representations of the three-point functions we calculate on the lattice. The top two diagrams are relevant for extracting matrix elements of the scalar density and temporal vector current, and the bottom diagram is calculated for the case $B_c \to D_s$ and the tensor current. Each operator insertion is shown by a cross and is labeled by its description given in the spin-taste basis, while the lines represent lattice quark propagators. The heavy quark propagator is represented by the line, labeled by the flavor h, between the leftmost operator and the insertion. The daughter quark propagator is represented by the line, labeled by the flavor $l(s)$, between the insertion and the rightmost operator. The remaining quark propagator is the spectator quark, labeled by the flavor c.

$\overline{\text{MS}}$ scheme. Nonperturbative (condensate) artifacts in Z_T in the RI-SMOM scheme are removed using the analysis of the J/ψ tensor decay constant [32].

D. Euclidean correlation functions on the lattice

We obtain the matrix elements discussed in Sec. II C from correlation functions on the lattice with ensembles and parameters specified in Sec. II B. We now describe the construction of these correlation functions.

To ensure that nonvanishing correlation functions are obtained when exclusively using staggered propagators in a heavy-HISQ calculation, operators at the source, sink and current insertion must be carefully selected so that the overall correlator is a taste singlet. As we detail in Sec. II E, matrix elements of the scalar density, vector current and tensor operator are extracted from three-point correlation functions whose constructions we now describe.

Our choice of operators used in the three-point correlation functions that we compute are given in Table IV and shown in Fig. 3. The operators are expressed in the staggered spin-taste basis. Note that the scalar density, temporal vector current and tensor operator all take the form $\Gamma \otimes \Gamma$ for some combination of gamma matrices Γ; thus, they are all local operators as discussed in Sec. II C.

TABLE IV. Summary of the interpolators used in the all-HISQ three-point correlation functions. The interpolators are given in the spin-taste basis. Matrix elements of the scalar density, vector current and tensor operator are extracted from the correlation functions constructed from the first, second and third rows of interpolators, respectively. The relevant form factor is given in the first column. The tensor form factor is calculated for $B_c \to D_s$ only here.

	H_c	$D_{l(s)}$	Insertion
f_0	$\gamma_5 \otimes \gamma_5$	$\gamma_5 \otimes \gamma_5$	$I \otimes I$
f_+	$\gamma_5\gamma_t \otimes \gamma_5\gamma_t$	$\gamma_5 \otimes \gamma_5$	$\gamma_t \otimes \gamma_t$
f_T	$\gamma_5\gamma_t \otimes \gamma_5\gamma_t$	$\gamma_5 \otimes \gamma_5\gamma_x$	$\gamma_x\gamma_t \otimes \gamma_x\gamma_t$

To extract the overlaps of the H_c and $D_{(s)}$ interpolators used in the three-point functions onto the low-lying pseudoscalar meson states, we compute the relevant two-point functions, namely, H_c with $\gamma_5 \otimes \gamma_5$ and $\gamma_5\gamma_t \otimes \gamma_5\gamma_t$ at both the source and sink, and $D_{(s)}$ with $\gamma_5 \otimes \gamma_5$ and $\gamma_5 \otimes \gamma_5\gamma_x$ at both the source and sink. The $D_{(s)}$ interpolator $\gamma_5 \otimes \gamma_5\gamma_x$ is the only nonlocal interpolator that we use.

We calculate the correlation functions needed to study the form factors for $B_c \to D_l$ and $B_c \to D_s$ together since the calculations share gluon field configurations and other lattice objects. From a computational perspective, these processes are similar since they both involve a charm quark which spectates a bottom quark that changes flavor. Hence, we are able to construct lattice correlation functions such that sequential b quark propagators, i.e., the combined bottom and charm propagator object, can be utilized in both calculations, thus saving us a computational expense.

E. Fitting correlation functions

The correlation functions are fit to the following forms using the *corrfitter* package [33]. The fit seeks to minimize an augmented χ^2 as described in [34–36].[1] We simultaneously fit all of the two-point and three-point correlation functions at all twists and heavy quark masses to account for all possible correlations between the fit parameters. We use singular value decomposition (SVD) cuts in our fits; thus, the $\chi^2/\text{d.o.f.}$ values from our fits of correlation functions do not have a straightforward interpretation in the sense of frequentist statistics. More discussions and details can be found in Appendix A 1. This includes details of our priors and a variety of tests of the stability of our fits.

The two-point correlator data are fit to the functional form

$$C_{2\text{pt}}(t) = \sum_i^{N_n} (a_{n,i})^2 f(E_{n,i}, t) - \sum_i^{N_o} (a_{o,i})^2 (-1)^t f(E_{o,i}, t)$$

$$(10)$$

---

[1]In the limit of high statistics the results from this method are equivalent to those from Bayesian inference.

where

$$f(E,t) = e^{-Et} + e^{-E(N_t - t)}. \tag{11}$$

This follows from the spectral decomposition of the Euclidean correlation functions. The sums over i enumerate the tower of states that have nonvanishing overlap with the interpolators such that $E_{n,i} \leq E_{n,i+1}$ and $E_{o,i} \leq E_{o,i+1}$. As is characteristic of staggered quarks, we find contributions to the correlation functions that switch signs between adjacent time slices. These contributions that oscillate with time are accounted for by the second piece in Eq. (10), where the subscript "o" is shorthand for "oscillating." Similarly, the subscript "n" in the first piece in Eq. (10) is shorthand for "nonoscillating." The function $f(E, t)$ accounts for the periodicity of the correlator data in the temporal direction. The amplitude $a_{n,0}$ is normalized such that

$$a_{n,0} = \frac{\langle 0 | \mathcal{O} | P \rangle}{\sqrt{2E_P}} \tag{12}$$

where $\mathcal{O}$ is the pseudoscalar meson interpolator, P is the low-lying pseudoscalar state, and $E_P = E_{n,0}$ is its energy.

The three-point data are fit to the functional form

$$\begin{aligned}
C_{3\text{pt}}(t, T) = & \sum_{i,j}^{N_n, N_n} a_{n,i} e^{-E_{n,i}t} V_{nn,ij} b_{n,j} e^{-E_{n,j}(T-t)} \\
& - \sum_{i,j}^{N_n, N_o} (-1)^{T-t} a_{n,i} e^{-E_{n,i}t} V_{no,ij} b_{o,j} e^{-E_{o,j}(T-t)} \\
& - \sum_{i,j}^{N_o, N_n} (-1)^t a_{o,i} e^{-E_{o,i}t} V_{on,ij} b_{n,j} e^{-E_{n,j}(T-t)} \\
& + \sum_{i,j}^{N_o, N_o} (-1)^T a_{o,i} e^{-E_{o,i}t} V_{oo,ij} b_{o,j} e^{-E_{o,j}(T-t)},
\end{aligned} \tag{13}$$

where the amplitudes a and b are the amplitudes in Eq. (10) corresponding to the initial and final pseudoscalar meson states in the three-point correlator.

For an insertion of the local scalar density, both source and sink operators are $\gamma_5 \otimes \gamma_5$. For an insertion of the temporal component of the local vector current, the $D_{l(s)}$ and H_c mesons are interpolated by $\gamma_5 \otimes \gamma_5$ and $\gamma_0\gamma_5 \otimes \gamma_0\gamma_5$, respectively. The matrix elements of the vector current and tensor operators are related to the fit parameters $V_{nn,ij}$ of the three-point functions through

$$\langle D_{l(s)} | J | H_c \rangle = Z V_{nn,00} \sqrt{2E_{D_{l(s)}} 2E_{H_c}}, \tag{14}$$

where J is the insertion that facilitates the $h \rightarrow l$ or s flavor transition and Z is the corresponding multiplicative renormalization factor for V or T. The pseudoscalar mesons of

interest are the lowest-lying states consistent with their quark content and the gamma matrix structure of the interpolators, so we only require extraction of the matrix elements for $i = j = 0$. The presence of $i, j > 0$ terms is necessary to give a good fit and allows for the full systematic uncertainty from the presence of excited states to be included in the extracted $V_{nn,00}$.

F. Fitting the form factors

From the parameters $V_{nn,00}$ in the fit form of the three-point correlation functions in Eq. (13), matrix elements are found using Eq. (14). The values of the form factors are then obtained by using Eqs. (7)–(9).

The form factor data at all momenta and heavy quark masses on all sets in Table I are then fit simultaneously to a functional form that allows for discretization effects, dependence on the heavy meson mass, and any residual mistuning of the light, strange and charm quark bare mass parameters. The fit is carried out using the *lsqfit* package [37], which implements a least-squares fitting procedure.

1. z-expansion

It is convenient, and now standard, to map the semileptonic region $m_\ell^2 < q^2 < t_- = (M_{H_c} - M_{D_{l(s)}})^2$ to a region on the real axis within the unit circle through

$$z(q^2) = \frac{\sqrt{t_+ - q^2} - \sqrt{t_+ - t_0}}{\sqrt{t_+ - q^2} + \sqrt{t_+ - t_0}}. \tag{15}$$

The parameter t_+ is chosen to be the threshold in q^2 for meson pair production with quantum numbers of the current [38], i.e., $(M_H + M_{\pi(K)})^2$. Any quark mass mistunings in our calculations are allowed by the fit function of the form factor data. In our $B_c \rightarrow D_l$ calculation, we determine the M_H value for evaluating t_+ from heavy-light two-point correlation functions that we fit simultaneously with the correlation functions described in Sec. II D. In our $B_c \rightarrow D_s$ calculation, which we analyze separately from $B_c \rightarrow D_l$, we estimate M_H by taking $M_H = M_{H_s} - (M_{B_s} - M_B)$. A similar approximation was taken in [3], a calculation of the form factors for $B_c \rightarrow J/\psi$. Also, we choose the parameter t_0 to be 0 so that the points $q^2 = 0$ and $z = 0$ coincide. The form factors can be approximated by a truncated power series in z. The validity of this truncation is scrutinized in Appendix B 3.

2. Fit form

Form factor data from our heavy-HISQ calculation is obtained, as described in Sec. II C, from matrix elements extracted from the fits detailed in Sec. II E. Data for each of the form factors are fit to the functional form

$$P(q^2)f(q^2) = \mathcal{L} \sum_{n=0}^{N_n} \sum_{r=0}^{N_r} \sum_{j=0}^{N_j} \sum_{k=0}^{N_k} A^{(nrjk)} \hat{z}^{(n,N_n)} \left(\frac{\Lambda}{M_{H_{l(s)}}}\right)^r \Omega^{(n)}$$
$$\times \left(\frac{am_h}{\pi}\right)^{2j} \left(\frac{am_c}{\pi}\right)^{2k} \mathcal{N}_{\mathrm{mis}}^{(n)}. \quad (16)$$

The dominant pole structure is represented by the factor $P(q^2)$ given by $1 - q^2/M_{\mathrm{res}}^2$. The values we use for M_{res}^2 are discussed in Sec. II F 3. The combination $P(q^2)f(q^2)$ is fitted to a truncated series, or polynomial, in $z(q^2)$ given in the rhs of Eq. (16). We use the Bourreley-Caprini-Lellouch (BCL) parametrization [39], where

$$\hat{z}_0^{(n,N_n)} = z^n,$$
$$\hat{z}_{+,T}^{(n,N_n)} = z^n - \frac{n(-1)^{N_n+1-n}}{N_n+1} z^{N_n+1} \quad (17)$$

in Eq. (16). We defined $z(q^2)$ in Eq. (15). The priors for $A^{(nrjk)}$ are taken to be 0(2) except for $j + k = 1$ where the prior is 0.0(3) to account for the removal of a^2 errors in the HISQ action at tree level [4]. In Appendix B 1, we show plots of the lattice data for $P(q^2)f(q^2)$ plotted against z in Figs. 25 and 26.

The factor $\mathcal{L}$ contains a chiral logarithm for the case $B_c \to D$, and we take $\mathcal{L} = 1$ for the case $B_c \to D_s$. For the case $B_c \to D$, then

$$\mathcal{L} = 1 + \left(\zeta^{(0)} + \zeta^{(1)}\frac{\Lambda}{M_{H_l}} + \zeta^{(2)}\frac{\Lambda^2}{M_{H_l}^2}\right) x_\pi \log x_\pi \quad (18)$$

where we take $\Lambda = 500$ MeV for the QCD energy scale, $x_\pi = M_\pi^2/\Lambda_\chi^2$, and $\Lambda_\chi = 4\pi f_\pi$ is the chiral scale. It is convenient for us to write x_π in terms of quark masses. By using $M_\pi^2 \approx m_l M_{\eta_s}^2/m_s$ and approximating the ratio $M_{\eta_s}/4\pi f_\pi$, we take $x_\pi = m_l/5.63 m_s^{\mathrm{tuned}}$ as in [40]. We give the coefficients ζ, common to all form factors, priors of 0(1).

The $(\Lambda/M_{H_{l(s)}})^r$ factors in Eq. (16) account for the dependence of the form factors on the heavy quark mass. This dependence is given by a HQET-inspired series in $\Lambda/M_{H_{l(s)}}$, which we truncate.

The $\Omega^{(n)}$ factors are given by

$$\Omega^{(n)} = 1 + \rho^{(n)}\log\left(\frac{M_{H_{l(s)}}}{M_{D_{l(s)}}}\right). \quad (19)$$

Here, $\Omega^{(n)}$ allows for heavy quark mass dependence that appears as a prefactor to the expansion in inverse powers of the heavy mass given in Eq. (16). From HQET this prefactor could include fractional powers of the heavy quark mass and/or logarithmic terms which vary in different regions of q^2 [41]. We allow for this with a logarithmic term with a variable coefficient that depends on the form

factor and the power of z in the z-expansion. We take priors for the $\rho^{(n)}$ of 0(1).

The kinematic constraint $f_0(0) = f_+(0)$ follows since the vector current matrix element must be finite at $q^2 = 0$. This constraint holds in the continuum limit for all M_{H_c}. Recalling that we choose $t_0 = 0$, which gives $z(0) = 0$, then this constraint is imposed on the fit by insisting that $(A_0)^{(0r00)} = (A_+)^{(0r00)}$ for all r and $\rho_0^{(0)} = \rho_+^{(0)}$.

The mistuning terms are given by

$$\mathcal{N}_{\mathrm{mis}}^{(n)} = 1 + \frac{\delta m_c^{\mathrm{sea}}}{m_c^{\mathrm{tuned}}}\kappa_1^{(n)} + \frac{\delta m_c^{\mathrm{val}}}{m_c^{\mathrm{tuned}}}\kappa_2^{(n)} + \frac{\delta m_l}{10 m_s^{\mathrm{tuned}}}\kappa_3^{(n)}$$
$$+ \frac{\delta m_s^{\mathrm{sea}}}{10 m_s^{\mathrm{tuned}}}\kappa_4^{(n)} + \frac{\delta m_s^{\mathrm{val}}}{10 m_s^{\mathrm{tuned}}}\kappa_5^{(n)}. \quad (20)$$

The parameters $\kappa_j^{(n)}$ allow for errors associated with mistunings of both sea and valence quark masses. For each of the sea and valence quark flavors, δm^{sea} and δm^{val} are given by

$$\delta m^{\mathrm{sea}} = m^{\mathrm{sea}} - m^{\mathrm{tuned}}$$
$$\delta m^{\mathrm{val}} = m^{\mathrm{val}} - m^{\mathrm{tuned}}, \quad (21)$$

giving estimates of the extent that the quark masses deviate from the ideal choices in which physical masses of hadrons are exactly reproduced. The $\delta m_s^{\mathrm{val}}$ term in $\mathcal{N}_{\mathrm{mis}}^{(n)}$ is not included for the $B_c \to D_l$ form factors since no valence strange quark is present in this case. For priors, we take 0(1) for those κ associated with valence quark mass mistunings, and 0.0(5) for sea quark mass mistunings, which are expected to have a smaller effect.

We now explain the specific values used for m^{tuned} for each flavor of quark. The tuned mass m_s^{tuned} is an estimate of the valence strange quark mass that would reproduce the "physical" η_s meson mass on the gauge field configurations we use. The η_s is a fictitious $s\bar{s}$ pseudoscalar meson where the valence strange quarks are prohibited from annihilating. It is not a particle that is realized in nature, though its mass can be determined in lattice QCD by ignoring disconnected diagrams. Hence, we use it as a tool to evaluate the extent to which the strange quark mass in simulations has been mistuned. We construct a physical value for the mass of the η_s meson ($M_{\eta_s}^{\mathrm{phys}}$) based on masses of pions and kaons [20]. We find am_s^{tuned} through

$$am_s^{\mathrm{tuned}} = am_s^{\mathrm{val}}\left(\frac{M_{\eta_s}^{\mathrm{phys}}}{M_{\eta_s}}\right)^2 \quad (22)$$

where am_s^{val} is the valence strange quark mass given in Table I, aM_{η_s} is taken from Table III of [6] (which also used our am_s^{val} values), and finally we use $M_{\eta_s}^{\mathrm{phys}} = 688.5(2.2)$ MeV from [20]. The value m_l^{tuned} is fixed by multiplying m_s^{tuned} from Eq. (22) by the physical ratio [24]

$$\frac{m_l}{m_s} = \frac{1}{27.18(10)}. \tag{23}$$

We take am_c^{tuned} to be

$$am_c^{\text{tuned}} = am_c^{\text{val}} \left(\frac{M_{J/\psi}^{\text{expt}}}{M_{J/\psi}} \right), \tag{24}$$

where $M_{J/\psi}^{\text{expt}} = 3.0969$ GeV (ignoring the negligible uncertainty) from PDG [42], and lattice values for $aM_{J/\psi}$ are obtained from Table III in [43] (which also used our am_c^{val} values). Thus, the tuned valence charm mass is designed to closely reproduce the physical mass of the J/ψ meson. A detailed discussion of tuning the valence charm quark mass can be found in [43].

3. Heavy quark mass dependence of M_{res}

For the f_0 and $f_{+,T}$ form factors, the relevant poles are the masses of the scalar and vector heavy-light(strange) mesons, respectively. Since these particles have a valence heavy quark, their masses vary with m_h. Determination of these meson masses at comparable precision to the energies of the pseudoscalar mesons is unnecessary. For the $J^P = 1^-$ mesons, this would require the set of correlation functions described in Sec. II E to be augmented by two-point correlation functions with propagators from different sources. Hence, additional propagators would need to be calculated. Instead, we approximate these meson masses similarly to the estimation of the $J^P = 0^+, 1^-$ heavy-charm mesons in [3,6] and the estimation of the $J^P = 0^+, 1^-$ heavy-strange mesons in [8].

Here, for $B_c \to D_{l(s)}$, we take the extra step in scrutinizing this method of approximating the masses of the $J^P = 0^+, 1^-$ mesons by demonstrating that our fits of the form factors are insensitive to shifts in these estimates. These checks are particularly important for processes facilitated by $b \to u$ or $b \to s$ since q_{max}^2 is close to M_{res}^2, so we expect the z coefficients in the fit form in Eq. (16) to be more sensitive to the position of the nearest pole. For example, $B_s \to D_s$ has $q_{\text{max}}^2 / M_{B_c^*}^2 = 0.29$ while $B_c \to D_s$ has $q_{\text{max}}^2 / M_{B_s^*}^2 = 0.63$ (with errors ignored). We show this analysis in Appendix B, which is summarized by Fig. 29.

We now show how we approximate masses of the heavy-light (strange) $J^P = 1^-$ and $J^P = 0^+$ mesons. We denote these mesons as $H_{l(s)}(1^-)$ and $H_{l(s)}(0^+)$. Similarly, in this section we refer to the pseudoscalar meson as $H_{l(s)}(0^-)$. The nearest pole for f_+ is the vector heavy-light (strange) vector meson. We use the fact that the hyperfine splittings

$$\Delta_{H_{l(s)}(1^-)} = M_{H_{l(s)}(1^-)} - M_{H_{l(s)}(0^-)} \tag{25}$$

are expected to vanish as Λ / m_h in the limit $m_h \to \infty$ [44] since, by HQET [45], there is a spin symmetry in this limit,

meaning that the vector and pseudoscalar mesons become degenerate. We model the leading order dependence on m_h through

$$M_{H_{l(s)}(1^-)} \approx M_{H_{l(s)}(0^-)} + \frac{x_{l(s)}}{M_{H_{l(s)}(0^-)}} \tag{26}$$

where $M_{H_{l(s)}}$ are proxies for m_h and the parameters $x_{l(s)}$ are set at $m_h = m_b$ using values from [28]; we take

$$x_{l(s)} = (M_{B_{l(s)}(1^-)} - M_{H_{l(s)}(0^-)}) M_{B_{l(s)}(0^-)} \tag{27}$$

so that the approximation in Eq. (26) yields $M_{H_{l(s)}(1^-)}$ equal to $M_{B_{l(s)}(1^-)}$ at $m_h = m_b$.

Regarding the pole for f_0, the differences between the pseudoscalar and scalar mesons,

$$\Delta_{l(s)}(m_h) = M_{H_{l(s)}(0^+)} - M_{H_{l(s)}(0^-)}, \tag{28}$$

are expected to be largely independent of the heavy quark mass because the scalar meson is simply an orbital excitation of the pseudoscalar meson. For example, note that $\Delta_s(m_b) = 0.344$ GeV and $\Delta_s(m_c) = 0.3490$ GeV (ignoring errors) are very similar [B_s, D_{s0} and D_s masses taken from [28] and B_{s0} mass taken from [46] (predicted)], providing qualitative support of this statement. Therefore, we approximate $M_{H_{l(s)}(0^+)}$ as

$$M_{H_{l(s)}(0^+)} \approx M_{H_{l(s)}(0^-)} + \Delta_{l(s)}(m_b). \tag{29}$$

The errors on $\Delta_{l(s)}(m_b)$ are ignored.

In Table V, we summarize the values of the masses that we use and subsequent values for x_l and x_s from Eq. (27). By construction, all of the heavy-light (strange) meson masses match the physical values (observed or predicted) at the point $m_h = m_b$.

In Eq. (16), the pole factor $P(q^2)^{-1}$ multiples a polynomial in z with degree N_n. For our final results, we use $N_n = 3$, i.e., a cubic polynomial in z. We demonstrate in Appendix B that results with $N_n = 4$ are in good agreement, and hence the truncation of the z series is justified.

TABLE V. Masses of the lightest mesons with J^P quantum numbers (given without error) in GeV [28,46,47] used for approximating the leading order dependence of the heavy quark mass on the location of the vector and scalar poles (see the text in Sec. II F 2). These values are also discussed in Appendix C. The parameter x is defined in Eq. (27), and the parameter $\Delta(m_b)$ is defined in Eq. (28).

	0^-	0^+	1^-	$\Delta(m_b)$ GeV	x GeV^2
$B_c \to D_l$	5.27964	5.627	5.324	0.34736	0.9368
$B_c \to D_s$	5.36684	5.711	5.4158	0.34416	1.0510

III. RESULTS

A. Form factors

We use the correlation function fits on each set indicated in Table IX of Appendix A 4. The energies and matrix elements on each set are stored (with all correlations) in the ancillary file `corrfit_results.tar` [10]. We fit the subsequent form factor data to the form described in Sec. II F 2. Fitting with noise added to both the data and priors, as demonstrated in [48] to compensate for the reduced χ^2/d.o.f. from fitting with a SVD cut, we find χ^2/d.o.f. = 0.65 and χ^2/d.o.f. = 0.43 for the cases $B_c \to D_l$ and $B_c \to D_s$, respectively.

We check that our priors are sensible and conservative by performing empirical Bayes analyses [34]. We use the `lsqfit.empbayes_fit` function to test the width of the parameters in the following two sets: $\rho^{(n)}$ and $A^{(nr00)}$, and $A^{(nrjk)}$ for $j + k > 0$. The widths of each parameter in these sets are varied simultaneously by a common multiplicative factor w. The empirical Bayes analyses show that the values for w are around 0.5, so our priors are moderately conservative.

In Fig. 4, we present our form factors in the limit of vanishing lattice spacing and physical quark masses across

FIG. 5. Fit functions for the four form factors $f_{0,+}^{l,s}$ tuned to the continuum limit with physical quark masses.

the entire physical range of q^2. Details of the fits of the correlation functions and lattice form factors from which Fig. 4 is derived are given in Appendixes A and B. Appendix C provides details of our form factors in the limit of vanishing lattice spacing and physical quark masses.

Figure 5 shows the form factors $f_{0,+}^{l,s}$ on the same plot. This figure shows how the form factors vary as the daughter quark mass changes from m_s to $m_l = m_s/27.4$. We plot each form factor from $q^2 = 0$ up to the zero-recoil point where $q^2 = (M_{B_c} - M_{D_{(s)}})$, which depends on the daughter quark mass. The form factors for the strange daughter quark are larger than those for the light daughter quark at all q^2 values. This mirrors what is seen, for example, in the comparison of $D \to \pi$ and $D \to K$ form factors [49].

For the case $B_c \to D_s$, we show in Fig. 6 the ratio $f_T(m_b)/f_+$ across the entire range of q^2. Large energy effective theory (LEET) [41] expects this ratio near $q^2 = 0$

FIG. 4. Fit functions for the $B_c \to D_l$ and $B_c \to D_s$ form factors $f_{0,+}^l$ and $f_{0,+,T}^s$, respectively, tuned to the continuum limit with physical quark masses. The tensor form factor is at the scale 4.8 GeV.
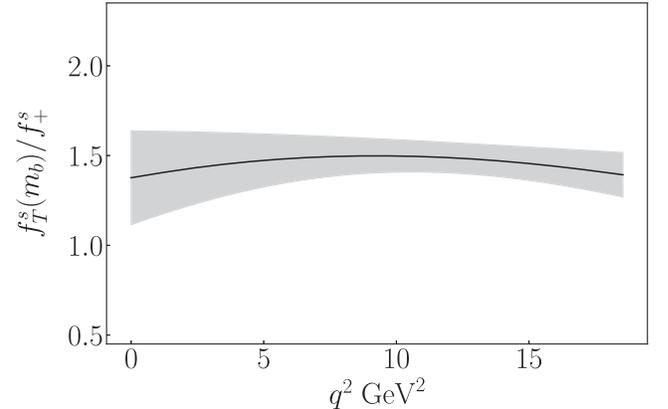
FIG. 6. Ratio of the tensor and vector form factors of $B_c \to D_s$ across the entire range of physical q^2. The behavior is in agreement with LEET [41], which predicts a constant ratio $(M_{B_c} + M_{D_s})/M_{B_c}$.
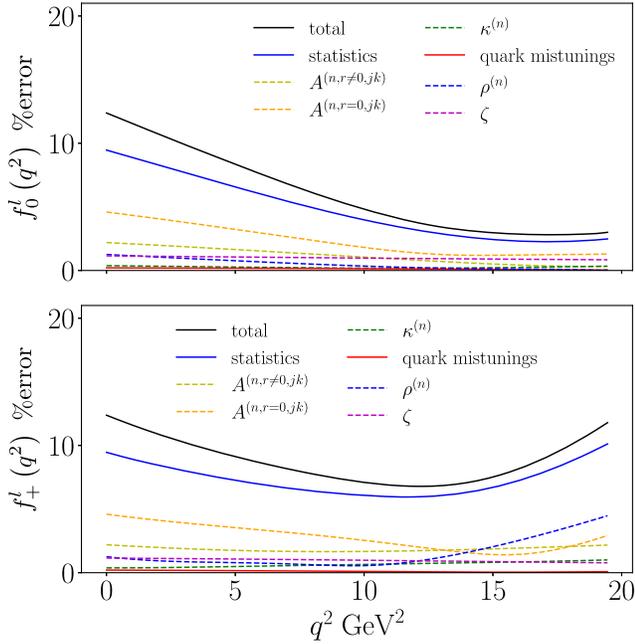
FIG. 7. Errors on the form factors $f_{0,+}^l$. The black curve shows the total error, and the other lines show a particular partition of the error. When added in quadrature, these contributions yield the black curve. The dashed curves show uncertainties from the fit coefficients in Eq. (16). The solid blue curve shows the statistical errors resulting from our fits of correlation functions. The solid red curve represents the contribution to the final error from the determinations of the quark mass mistunings on each lattice [see Eq. (20)].

FIG. 8. Errors on the form factors $f_{0,+,T}^s$. The curves are labeled similarly to Fig. 7.

to take the value $(M_{B_c} + M_{D_s})/M_{B_c} = 1.31$ [28] in the limit $m_b \to \infty$, ignoring renormalization corrections. This follows from the spatial-temporal tensor and spatial vector matrix elements coinciding in the limits $m_b \to \infty$ and $q^2 \to 0$, and the definitions of f_+ and f_T in Eqs. (8) and (9). We find that the ratio f_T/f_+ near $q^2 = 0$ is consistent with LEET and that this ratio does not change significantly as q^2 is varied.

We use the *gvar* package [50] to propagate correlations throughout our calculation. The package also allows us to decompose the uncertainty on the form factors and resulting branching fractions to create an error budget. We plot a particular breakdown of the errors in Figs. 7 and 8 for the form factors $f_{0,+}^l$ and $f_{0,+}^s$, respectively. We find that statistical errors contribute substantially to the final error. Of a similar size are the uncertainties from the coefficients $A^{(n0jk)}$ in the fit form in Eq. (16). The fit function in Eq. (16) is complicated since the coefficients $A^{(nrjk)}$ responsible for the extrapolations $am_h \to 0$, $am_c \to 0$ and $\Lambda/M_{H_{l(s)}} \to \Lambda/M_{B_{l(s)}}$ are mixed to allow for all possible effects. Terms in the fit form with $r = 0$ are associated with discretization effects of the leading order term in the HQET expansion. This error could be decreased by including the exafine lattice ($a \approx 0.03$ fm) so that am_h can be taken smaller to further

constrain the limit $am_h \to 0$. Also, b quarks, at their physical mass, can be directly simulated on the exafine lattice since am_b is well below 1. We investigate the impact of adding the exafine lattice in Sec. IV A.

Regarding the ζ and ρ parameters in Eq. (16), only $\zeta^{(0)}$ and $(\rho^{l,s})^{(0)}$ are determined accurately by the fit. We find $\zeta^{(0)} = -0.66(24)$, $(\rho_{0,+}^l)^{(0)} = -0.544(76)$, $(\rho_{0,+}^s)^{(0)} = -0.579(64)$ and $(\rho_T^s)^{(0)} = -0.676(92)$.

B. Observables for $B_c^+ \to D^0 \ell^+ \nu_\ell$

We plot the differential decay rate $\eta_{\rm EW}^{-2} |V_{ub}|^{-2} d\Gamma(B_c^+ \to D^0 \ell^+ \nu_\ell)/dq^2$ derived from our form factors as a function of q^2 in Fig. 9. The form of the decay rate is given in Eq. (2). We integrate this function (using gvar.ode.integral in the *gvar* package [50]) to find $\eta_{\rm EW}^{-2} |V^{ub}|^{-2} \Gamma$. This is then combined with $\eta_{\rm EW}$, the CKM matrix element $V_{ub} = 3.82(24) \times 10^{-3}$ [51] (an average of inclusive and exclusive determinations), and the lifetime of the B_c meson to obtain the branching ratios in Table VI. At present, errors from our lattice calculation dominate those associated with the lifetime of the B_c meson and are comparable with those
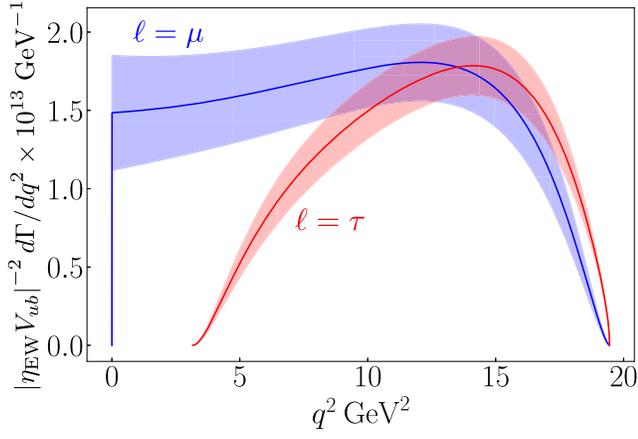
FIG. 9. Differential decay rate $\eta_{\rm EW}^{-2}|V^{ub}|^{-2}d\Gamma(B_c^+ \to D^0\ell^+\nu_\ell)/dq^2$ as a function of q^2 for the cases $\ell = \mu$ in blue and $\ell = \tau$ in red.

from the CKM element V_{ub}. For the ratio of widths with τ and μ in the final state, we find that

$$\frac{\Gamma(B_c^+ \to D^0\tau^+\nu_\tau)}{\Gamma(B_c^+ \to D^0\mu^+\nu_\mu)} = 0.682(37). \qquad (30)$$

Much of the error on our form factors cancels in this ratio, and we achieve an uncertainty of 7%.

We compare our results with those for the decay mode $B_c^+ \to J/\psi\ell^+\nu_\ell$. We take the form factors for this decay from HPQCD's lattice QCD calculation in [3]. We combine these form factors with those for $B_c^+ \to D^0\ell^+\nu_\ell$ computed in this study to find the ratios

$$\left|\frac{V_{cb}}{V_{ub}}\right|^2 \frac{\Gamma(B_c^+ \to D^0\mu^+\nu_\mu)}{\Gamma(B_c^+ \to J/\psi\mu^+\nu_\mu)} = 0.257(36)(18),$$

$$\left|\frac{V_{cb}}{V_{ub}}\right|^2 \frac{\Gamma(B_c^+ \to D^0\tau^+\nu_\tau)}{\Gamma(B_c^+ \to J/\psi\tau^+\nu_\tau)} = 0.678(69)(45). \qquad (31)$$

The first error comes from our form factors for $B_c^+ \to D^0\mu^+\nu_\mu$, and the second error comes from the form factors for $B_c^+ \to J/\psi\mu^+\nu_\mu$ in [3]. We treat the form factors

TABLE VI. For $B_c^+ \to D^0\ell^+\nu_\ell$, we give values for the branching ratios (BR) for each of the cases $\ell = e$, μ, τ. We take the lifetime of the B_c meson to be 513.49(12.4) fs [52]. The errors from the lifetime and the CKM matrix element V_{ub} are shown explicitly. The error from $\eta_{\rm EW}$ is negligible. We ignore uncertainties from long-distance QED contributions since the meson D^0 in the final state is neutral.

Decay mode	BR $\times 10^5$
$B_c^+ \to D^0 e^+\nu_e$	$3.37(48)_{\rm lattice}(8)_{\tau_{B_c}}(42)_{\rm CKM}$
$B_c^+ \to D^0\mu^+\nu_\mu$	$3.36(47)_{\rm lattice}(8)_{\tau_{B_c}}(42)_{\rm CKM}$
$B_c^+ \to D^0\tau^+\nu_\tau$	$2.29(23)_{\rm lattice}(6)_{\tau_{B_c}}(29)_{\rm CKM}$
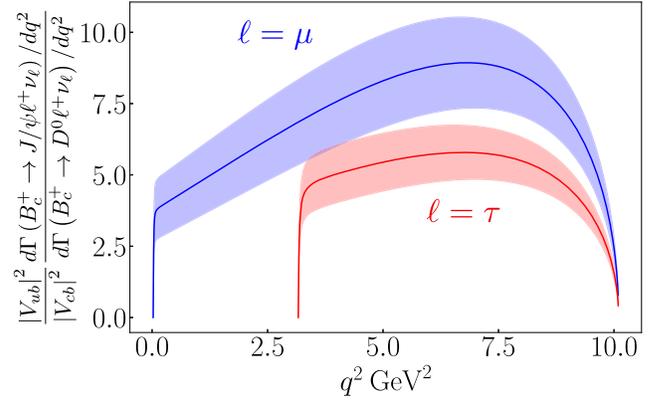
FIG. 10. We plot the ratio of $d\Gamma/dq^2$ for each of the processes $B_c^+ \to J/\psi\ell^+\nu_\ell$ and $B_c^+ \to D^0\ell^+\nu_\ell$ for the q^2 range of the $B_c^+ \to J/\psi\ell^+\nu_\ell$ decay. The decay width for the former process is derived from form factors found in [3], and the decay width of the latter process is derived from form factors determined in this study. The case $\ell = \mu$ is shown in blue, and the case $\ell = \tau$ is shown in red.

for $B_c^+ \to J/\psi\mu^+\nu_\mu$ as uncorrelated to the $B_c^+ \to D^0\ell^+\nu_\ell$ form factors (a conservative strategy). In Fig. 10, we plot the ratio of $d\Gamma/dq^2$ for the two processes for $m_\ell^2 < q^2 < (M_{B_c} - M_{J/\psi})^2$ and each of the cases $\ell = \mu$, τ. Note that the ratio plotted is the inverse of the one used in Eq. (31).

A possible method for determining the ratio of $|V_{cs}|/|V_{ub}|$ is to determine the ratio of branching fractions for the B_c decay to $D^0e^+\nu_e$ and $B_se^+\nu_e$. Using our form factors for $B_c \to D$ and the form factors for $B_c \to B_s$ from [7], we find

$$\frac{|V_{ub}|^2}{|V_{cs}|^2} \frac{\mathcal{B}(B_c^+ \to B_s^0 e^+\nu_e)}{\mathcal{B}(B_c^+ \to D^0 e^+\nu_e)} = 5.95(84)(19) \times 10^{-3}. \qquad (32)$$

References [53,54] point out that the weak matrix elements for $B_c \to D$ and $B_c \to B_s$ have a simple ratio at the zero-recoil point in the limit of $m_b \gg m_c \gg \Lambda_{\rm QCD}$. In this limit, the B_c meson is a pointlike particle, and the weak matrix elements factorize into a factor that depends on the daughter meson decay constant and a factor that depends on the B_c wave function, which is the same in both processes. Thus, the ratio of weak matrix elements becomes

$$\frac{\langle D|V_\mu|B_c\rangle}{\langle B_s|V_\mu|B_c\rangle}\bigg|_{\rm zero-recoil} = \frac{M_D f_D}{M_{B_s} f_{B_s}}. \qquad (33)$$

Using the decay constants from [24], the rhs evaluates to 0.32. We expect an uncertainty on this value of size $\Lambda_{\rm QCD}/m_c$ ($\sim$30%) since the HQET result relies on $m_c \gg \Lambda_{\rm QCD}$. By using our form factors for $B_c \to D$ and those for $B_c \to B_s$ from [7], we find that the lhs evaluates to 0.571(17)(8), much larger than the prediction from HQET. We conclude that HQET is not a reliable guide here. Calculations from three-point sum rules [54] give 0.5(2).

We now give the angular dependence of the differential decay rate. Let θ be the angle between the direction of flight of the lepton $\bar{\ell}$ and the D^0 meson in the center-of-mass frame of $\bar{\ell}\nu$. Then, we have

$$\frac{d^2\Gamma_\ell(q^2,\cos\theta)}{dq^2 d\cos\theta} = a_\ell(q^2) + b_\ell(q^2)\cos\theta + c_\ell(q^2)\cos^2\theta.$$

$$(34)$$

On performing the integration with respect to θ, the piece linear in $\cos\theta$ vanishes, though it is of interest when studying the angular dependence of the decay width. This forward-backward asymmetric piece, $b_\ell(q^2)$, is sensitive to the lepton mass. It is given by

$$b_\ell(q^2) = -\frac{\eta_{\text{EW}}^2 G_F^2 |V_{ub}|^2 |\mathbf{q}|}{64\pi^3 M_{B_c}^2}\left(1 - \frac{m_\ell^2}{q^2}\right)^2 \frac{m_\ell^2}{q^2}$$
$$\times \lambda(M_{B_c}^2, M_D^2, q^2)^{1/2}(M_{B_c}^2 - M_D^2)f_0(q^2)f_+(q^2)$$

$$(35)$$

where $\lambda(x^2,y^2,z^2) = [x^2-(y-z)^2][x^2-(y+z)^2]$. In Fig. 11, we plot $b_\ell(q^2)$ for the cases $\ell = \mu, \tau$. The shape of $b_\ell(q^2)$ differs between the two cases. To exhibit in more detail the low-q^2 behavior of $b_\mu(q^2)$, we separately plot the regions $q^2 < 1$ GeV^2 and 1 GeV$^2 \leq q^2$.

C. Observables for $B_c^+ \rightarrow D_s^+ \ell^+ \ell^-$ and $B_c^+ \rightarrow D_s^+ \nu\bar{\nu}$

Like $B \rightarrow K\ell^+\ell^-$, the process $B_c^+ \rightarrow D_s^+\ell^+\ell^-$ is a rare decay mediated by the loop-induced $b \rightarrow s$ transition. Here, we follow nomenclature commonly used for $B \rightarrow K\ell^+\ell^-$ as in [55] and replace the initial and final mesons in the $B \rightarrow K$ formulas with B_c and D_s, respectively. We calculate observables for $B_c^+ \rightarrow D_s^+\ell^+\ell^-$ from our form factors $f_{0,+,T}^s$ ignoring small nonfactorizable contributions at low q^2 [56,57].

We use the same value for $|V_{tb}V_{ts}^*| = 0.0405(8)$ [58] and the Wilson coefficients in [12]. The Wilson coefficients used in [12] are quoted at the scale 4.8 GeV.

The determination of the branching fraction includes effective Wilson coefficients expressed in terms of the functions $h(q^2, m_c)$ and $h(q^2, m_b)$ that depend on the c and b pole masses. We take m_c and m_b in the $\overline{\text{MS}}$ scheme to be 1.2757(84) GeV [59] and 4.209(21) GeV [60], respectively, each at their own scale. Using the 3-loop expression in Eq. (12) of [61] that relates the pole mass to the mass in the $\overline{\text{MS}}$ scheme, we find the values 1.68 GeV and 4.87 GeV for the pole mass of the charm and bottom quarks, respectively, each taken with an uncertainty of 200 MeV to account for the presence of a renormalon in the pole mass [62] suffered by the perturbation series in the expression in [61].

In Fig. 12, we plot the differential branching fractions for the cases $\ell = \mu, \tau$ for the physical range
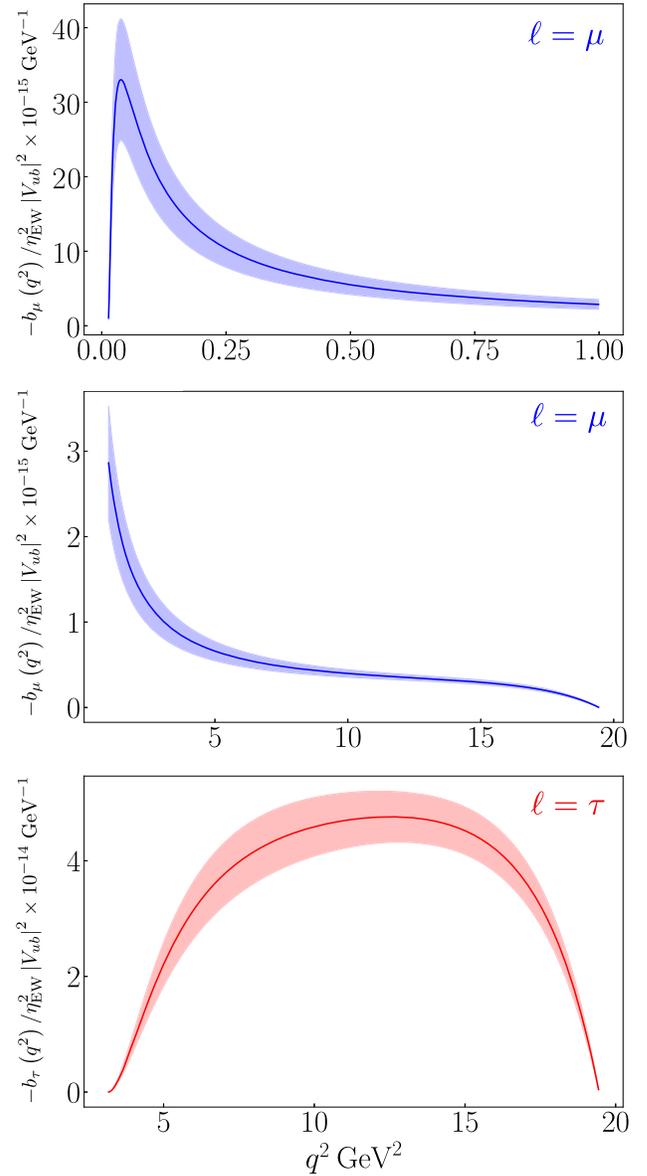
FIG. 11. Plot of the $b_\ell(q^2)$, as defined in Eqs. (35) and (34), for $B_c^+ \rightarrow D_s^+\ell^+\ell^-$. The top plot shows the case $\ell = \mu$ (blue) for the region $m_\mu^2 < q^2 < 1$ GeV^2. The middle plot shows the case $\ell = \mu$ (blue) for the region 1 GeV$^2 < q^2 < q_{\text{max}}^2$. Finally, the lower plot shows the case $\ell = \tau$ (red).

$4m_\ell^2 < q^2 < (M_{B_c} - M_{D_s})^2$. These are constructed from the expressions in [55] for $B \rightarrow K$. The yellow bands span across $\sqrt{q^2} = 2.956$–3.181 GeV and 3.586–3.766 GeV. These regions are the same as in [63], and they represent veto regions which largely remove contributions from charmonium resonances via intermediate J/ψ and $\psi(2S)$ states. The effects of charmonium resonances are not included in our differential branching fractions. For $d\mathcal{B}_\mu/dq^2$ between $\sqrt{q^2} = 2.956$ and $\sqrt{q^2} = 3.766$, we interpolate the function linearly as performed in [64] for the $B \rightarrow K$ branching fraction.
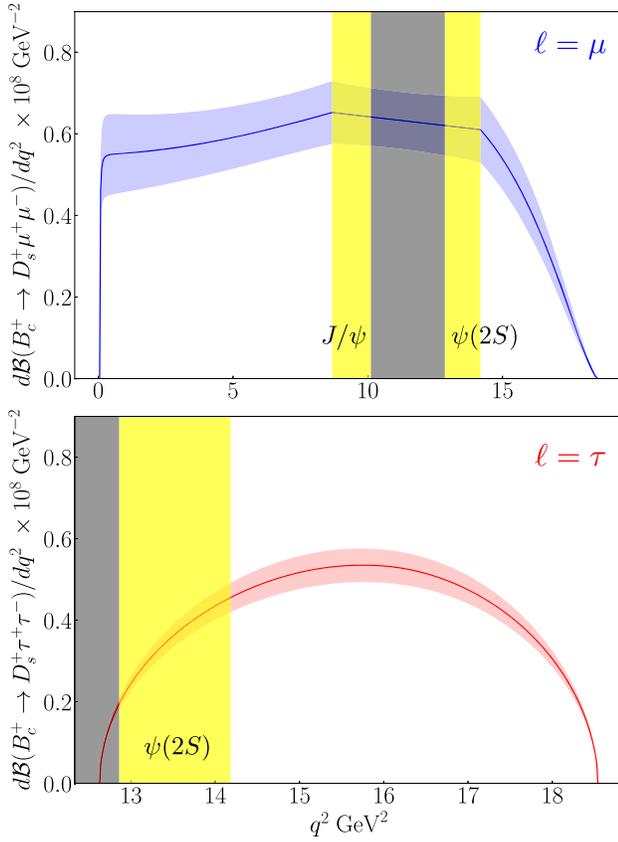
FIG. 12. Plot of the $B_c^+ \to D_s^+ \ell^+ \ell^-$ differential branching ratio for $\ell = \mu$ (top) and $\ell = \tau$ (bottom) in the final state. The yellow bands show regions where charmonium resonances (not included in our calculation) could have an impact. The grey band is between the two yellow regions labeling the charmonium resonances. Through the yellow and gray bands, we interpolate the function $d\mathcal{B}_\mu/dq^2$ linearly when integrating to find the branching fraction and related quantities.

On integrating with respect to q^2, we report the ratio

$$R_{\ell_2}^{\ell_1}(q_{\text{low}}^2, q_{\text{high}}^2) = \frac{\int_{q_{\text{low}}^2}^{q_{\text{high}}^2} dq^2 d\mathcal{B}_{\ell_1}/dq^2}{\int_{q_{\text{low}}^2}^{q_{\text{high}}^2} dq^2 d\mathcal{B}_{\ell_2}/dq^2} \tag{36}$$

for different choices of final-state lepton $\ell_{1,2}$ and integration limits q_{low}^2, q_{high}^2. We find that

$$R_e^\mu(4m_\mu^2, q_{\text{max}}^2) = 1.00203(47), \tag{37}$$

$$R_e^\mu(1 \text{ GeV}^2, 6 \text{ GeV}^2) = 1.00157(52), \tag{38}$$

$$R_e^\mu(14.18 \text{ GeV}^2, q_{\text{max}}^2) = 1.0064(12), \tag{39}$$

$$R_e^\tau(14.18 \text{ GeV}^2, q_{\text{max}}^2) = 1.34(13), \tag{40}$$

$$R_\mu^\tau(14.18 \text{ GeV}^2, q_{\text{max}}^2) = 1.33(13), \tag{41}$$

TABLE VII. For $B_c^+ \to D_s^+ \ell^+ \ell^-$, we give values for $d\mathcal{B}/dq^2 \times 10^7$ integrated with respect to q^2 over the given ranges $(q_{\text{low}}^2, q_{\text{high}}^2)$ in GeV^2 for each of the cases $\ell = e, \mu, \tau$. We take the lifetime of the B_c meson to be 513.49(12.4) fs [52]. Note that these results do not include effects from charmonium or $u\bar{u}$ resonances.

Decay mode	$(4m_\ell^2, q_{\text{max}}^2)$	$(1,6)$	$(14.18, q_{\text{max}}^2)$
$B_c^+ \to D_s^+ e^+ e^-$	1.00(11)	0.285(41)	0.146(22)
$B_c^+ \to D_s^+ \mu^+ \mu^-$	1.00(11)	0.286(41)	0.147(22)
$B_c^+ \to D_s^+ \tau^+ \tau^-$	0.245(18)	...	0.195(14)

where $q_{\text{max}}^2 = (M_{B_c} - M_{D_s})^2$. The latter three ratios above involve the differential decay widths above the veto region associated with the resonance from $\psi(2S)$. The ratio in Eq. (38) lies beneath the J/ψ veto region and above $q^2 \lesssim 1$ GeV^2 where effects from $u\bar{u}$ resonances could have an impact; these are not included in our calculation. We give in Table VII integrals of differential branching fractions for these ranges of q^2. As in the case $B_c^+ \to D^0 \ell^+ \nu_\ell$, the ratio of widths with $\ell = \tau$ and $\ell = \mu$ in the final state,

$$\frac{\Gamma(B_c^+ \to D_s^+ \tau^+ \tau^-)}{\Gamma(B_c^+ \to D_s^+ \mu^+ \mu^-)} = 0.245(20), \tag{42}$$

has reduced error.

In the low-q^2 region 1 GeV^2 to 6 GeV^2, we find that the ratio of integrated branching fractions for $B_c^+ \to D_s^+ \mu^+ \mu^-$ and $B_c^+ \to J/\psi \mu^+ \nu_\mu$ is

$$\frac{\int_{1 \text{ GeV}^2}^{6 \text{ GeV}^2} dq^2 \frac{d\mathcal{B}(B_c^+ \to D_s^+ \mu^+ \mu^-)}{dq^2}}{\int_{1 \text{ GeV}^2}^{6 \text{ GeV}^2} dq^2 \frac{d\mathcal{B}(B_c^+ \to J/\psi \mu^+ \nu_\mu)}{dq^2}} = 6.31(90)(65) \times 10^{-6}. \tag{43}$$

The first error is from the numerator, and the second error is from the denominator, which we compute using the form factors for $B_c^+ \to J/\psi \mu^+ \nu_\mu$ from [3]. As in [3], we take $|V_{cb}| = 41.0(1.4) \times 10^{-3}$ [65] from an average of inclusive and exclusive determinations, scaling the uncertainty by 2.4 to allow for their inconsistency.

Next, we show in Fig. 13 the "flat term" F_H^ℓ, first introduced in [66] in the context of $B \to K$. This term appears as a constant in the angular distribution of the decay width. Taking the same parametrization of the decay width as in Eq. (34), then performing the integration with respect to q^2, we have

$$\frac{1}{\Gamma_\ell} \frac{d\Gamma_\ell(\cos\theta)}{d\cos\theta} = \frac{3}{4}(1 - F_H^l)(1 - \cos^2\theta) + \frac{1}{2}F_H^\ell + A_{\text{FB}}^\ell \cos\theta \tag{44}$$

where

FIG. 14. Differential branching fraction for $B_c^+ \to D_s^+ \nu\bar\nu$ as a function of q^2.

The flat term F_H^ℓ may be sensitive to contributions from new physics since it is small according to the Standard Model. This quantity is a ratio of combinations of the form factors, and uncertainties are much less than those exhibited by the raw form factors or branching fractions.

We determine the differential branching fraction for $B_c^+ \to D_s^+ \nu\bar\nu$ using the expressions for the $B \to K\nu\bar\nu$ case in [13,14]. The differential branching fraction, summing over the three neutrino flavors, is

$$\frac{d\mathcal{B}(B_c^+ \to D_s^+ \nu\bar\nu)}{dq^2} = \tau_{B_c} |V_{tb}V_{ts(d)}^*|^2 \frac{G_F^2 \alpha^2}{32\pi^5} \frac{X_t^2}{\sin^4\theta_W} \times |\boldsymbol{q}|^3 f_+^2(q^2) \tag{48}$$

which we plot in Fig. 14. We take $X_t = 1.469(17)$ [67] and $\alpha^{-1}(M_Z) = 127.952(9)$ [65]. Integrated from $q^2 = 0$ to q_{max}^2, we find the branching fraction

$$\mathcal{B}(B_c^+ \to D_s^+ \nu\bar\nu) = 8.23(85) \times 10^{-7}. \tag{49}$$

There are no issues from charmonium resonances or nonfactorizable pieces in this case. Since $m_\tau > M_{D_s}$, there is also no long-distance contribution for the τ case (unlike for $B \to K\nu_\tau\bar\nu_\tau$). We find the ratio of branching fractions

$$\frac{\mathcal{B}(B_c^+ \to D_s^+ \nu\bar\nu)}{\mathcal{B}(B_c^+ \to J/\psi\mu^+\nu_\mu)} = 5.49(57)(55) \times 10^{-5}. \tag{50}$$

The first error is from the numerator, and the second error is from the denominator, which we compute using the form factors for $B_c^+ \to J/\psi\mu^+\nu_\mu$ from [3].

FIG. 13. From top to bottom, we show plots of the flat terms F_H^ℓ for each of $\ell = e, \mu, \tau$, respectively. We use a log scale for the cases $\ell = e, \mu$. Error bands are presented, though the errors are small due to the correlations in the construction of the flat term.

$$A_{FB}^\ell = \frac{1}{\Gamma_\ell} \int_{q_{min}^2}^{q_{max}^2} dq^2 b_\ell(q^2), \tag{45}$$

$$F_H^\ell = \frac{2}{\Gamma_\ell} \int_{q_{min}^2}^{q_{max}^2} dq^2 (a_\ell(q^2) + c_\ell(q^2)), \tag{46}$$

and we define

$$F_H^\ell(q^2) = \frac{2(a_\ell(q^2) + c_\ell(q^2))}{2a_\ell(q^2) + \frac{2}{3}c_\ell(q^2)}. \tag{47}$$

IV. FUTURE PROSPECTS: IMPROVING ACCURACY OF THE FORM FACTORS

We consider two extensions to our current strategy to improve uncertainties in the future: the addition of a finer lattice and the inclusion of the spatial vector current.

A. Simulating with a physically massive *b* quark on the exafine lattice

We carry out the first heavy-to-light decay analysis on the exafine gluon field configurations, with size $N_x^3 \times N_t = 96^3 \times 288$ and lattice spacing $a \approx 0.033$ fm. These configurations are finer than all the sets used in our calculation thus far. The lattice spacing is such that $am_b \approx 0.625$; therefore, we are able to simulate with physically heavy *b* quarks on this lattice with reasonably small discretization effects associated with am_h.

Computations on the exafine lattices are expensive due to the large size, $N_x^3 \times N_t$. Hence, since these investigations are preliminary, we restrict the calculation to $B_c \rightarrow D_s$ and compute with a small selection of parameters on 100 configurations, each with 4 different positions of a random wall source. We take $am_h = 0.35, 0.625$ and calculate with three different momenta (including zero recoil), plus a further larger momentum for $am_h = 0.625$: a three-momentum transfer of roughly 2.8 GeV.

In Fig. 15, we show form factor results on the exafine lattice with these two masses along with our physical-continuum curve at $m_h = m_b$ derived from the coarser lattices (presented in Sec. III A). The exafine data at $am_h = 0.625$ closely follow the physical-continuum curve.

Errors on the physical-continuum form factors from fits with and without the data from the exafine lattice are shown in Table VIII. From this table, we see that errors are reduced by 15%–25% at zero recoil on inclusion of data on the exafine lattice.

Given our present statistics on the exafine lattice, we are able to cover at least half the range of q^2 with reasonable errors. Reducing the uncertainties at lower q^2 values will require higher statistics; however, data on exafine with $q^2 > q_{\max}^2/2$ give some error reduction at $q^2 = 0$.

B. Extracting f_+ from matrix elements of the spatial vector current

As can be clearly seen in Figs. 23–26 in Appendix B, the errors on the lattice data for f_+ near zero recoil (maximum q^2) are much larger than the errors seen away from zero recoil. This is not because our extraction of the matrix elements $\langle D_{l(s)}|S_{\mathrm{local}}|H_c\rangle$ and $\langle D_{l(s)}|V^0_{\mathrm{local}}|H_c\rangle$ is especially imprecise at these momenta, but because we extract the form factor via Eq. (8). The denominator in Eq. (8) approaches zero as q^2 approaches $q_{\max}^2$. However, f_+ is finite and analytic at $q_{\max}^2$, so the numerator also vanishes at $q_{\max}^2$. In practice, the smallness of both the numerator and the denominator at large q^2 results in a large error for the
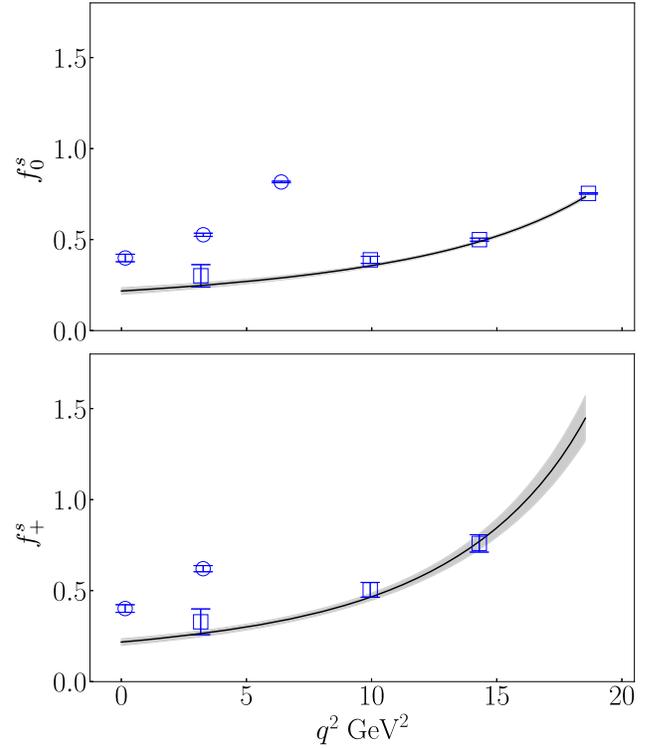
FIG. 15. We show data from the exafine lattice in blue with squares, denoting $am_h = 0.625$, and circles, denoting $am_h = 0.35$. Alongside the exafine data, we show the fits of the form factors f_0^s (top) and f_+^s (bottom) from ultrafine sets to coarser sets as presented in the upper plot of Fig. 4. The lattice data at $am_h = 0.625$ ($\approx am_b$) closely follow the fit curves.

extracted value of f_+. As a consequence, the error on the final physical-continuum form factor f_+ is large, certainly larger than the error on f_0 at zero recoil.

We now propose and investigate a method to reduce the error on f_+ near zero recoil. For these purposes, we consider only the process $B_c \rightarrow D_s$. As an alternative to extracting f_+ via Eq. (8), we set $\mu = i \neq 0$ in Eq. (1) to find

$$f_+^s(q^2) = \frac{-q^2 Z_V \langle D_s|V^i|H_c\rangle/q^i + f_0^s(q^2)(M_{H_c}^2 - M_{D_s}^2)}{q^2 + M_{H_c}^2 - M_{D_s}^2}$$

(51)

TABLE VIII. Comparison of extremal values of the form factors in the physical-continuum limit. The second column gives results from our fit without any data points on the exafine lattice. The third column gives results using the same fit form but now including results on the exafine lattice. Errors are reduced from the second to the third column.

	Without exafine	With exafine
$f_{0,+}^s(0)$	0.217(18)	0.221(16)
$f_0^s(q_{\max}^2)$	0.736(11)	0.7383(91)
$f_+^s(q_{\max}^2)$	1.45(12)	1.433(97)
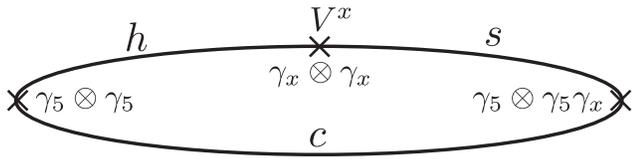
FIG. 16. Diagrammatic representation of the three-point functions we calculate on set 1 for insertions of the local spatial vector current $\gamma_x \otimes \gamma_x$ as described in the text in Sec. IV B. Each operator is shown by a cross and is labeled by its description given in the spin-taste basis, while the lines represent lattice quark propagators as in Fig. 3.

which, in addition to the matrix elements calculated in our existing setup, involves matrix elements of a spatial component of the vector current.

To achieve this we include the three-point function given in Fig. 16 where the spatial vector current has spin-taste $\gamma_x \otimes \gamma_x$. This correlation function has the advantage that the spatial vector current has the same multiplicative renormalization as for the $\gamma_t \otimes \gamma_t$ insertion in the middle diagram of Fig. 3 (up to discretization effects handled when fitting the form factor data).

To demonstrate the effectiveness of extracting f_+ via Eq. (51) versus the extraction of f_+ via Eq. (8), we apply the method outlined above to set 1 in Table I. In Fig. 17, we show lattice data for f_+ from the different methods of extraction.

From Fig. 17, we see that the different extractions are in excellent agreement and that the improvement in accuracy of the lattice data for f_+ by using Eq. (51) is very large close to zero recoil (maximum q^2). By utilizing the spatial vector current, we observe errors near zero recoil
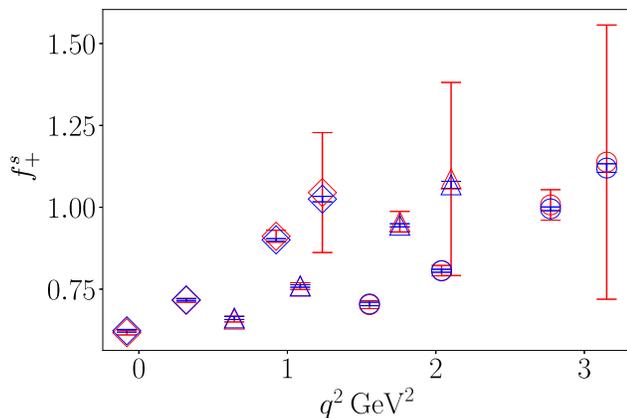
FIG. 17. Lattice data on set 1 (see Table I) for f_+^s for different methods of extraction which we differentiate by color. The blue points are the f_+^s data extracted via Eq. (51) using the local spatial vector current $\gamma_x \otimes \gamma_x$. The red points are the f_+^s data extracted via Eq. (8) using the local temporal vector current. The blue and red points agree very well at all q^2. Near zero recoil, the errors on blue points are much smaller than the red points.

comparable to those seen at momenta further away from maximum q^2. Hence, using this approach on all lattices, we can expect an error on the physical-continuum f_+ form factor near zero recoil comparable to that seen for f_0. Therefore, by including matrix elements of the spatial vector current, we expect errors on our physical-continuum f_+ form factor at zero recoil to reduce roughly by a factor of 2.

V. CONCLUSIONS AND OUTLOOK

For the first time from lattice QCD, we obtain the scalar and vector form factors $f_{0,+}$ for $B_c \to D_l$, and the scalar, vector and tensor form factors $f_{0,+,T}$ for $B_c \to D_s$ across the entire physical ranges of q^2 in the continuum limit with physical quark masses. Our lattice QCD calculation uses four different lattices with three different lattice spacings, both unphysically and physically massive light quarks, and a range of heavy quark masses. Together, the lattice data inform the limit of vanishing lattice spacing, physical b quark mass, and physical (equal-mass) up and down quark masses. The reader should consult Appendix C for instructions on how to reconstruct our form factors.

The error on the decay widths $\Gamma(B_c^+ \to D^0 \ell^+ \nu_\ell)$ (see Table VI) from our form factors is similar to the error on the present determination of V_{ub}. For the cases $\ell = e$ or μ, the lattice error is 13% larger than the error from V_{ub}, whereas, for $\ell = \tau$, the lattice error is nearly 20% smaller than the error from V_{ub}. The error on the form factors calculated here for $B_c \to D_s$ is smaller than that for $B_c \to D$ by up to a factor of 2 at small recoil.

Experimental observations are expected from LHC in the near future [68]. In Secs. III B and III C we give results for a host of observables that can be compared to experiment. In Sec. IV we demonstrate how the uncertainties in our calculation can be reduced in the future to complement experimental results as they improve.

APPENDIX A: CORRELATOR FITTING ANALYSIS

1. Method

As described in Sec. II E, we fit our two- and three-point correlation functions to the fit forms given in Eqs. (10) and (13). We minimize the usual χ^2,

$$\chi^2 = \sum_{i,j} (f(x_i; p) - y_i)(\sigma^y)^{-2}_{ij} (f(x_j; p) - y_j) \quad \text{(A1)}$$

with the additional piece

$$\chi^2_{\text{prior}} = \sum_a \left(\frac{p_a - p_a^{\text{prior}}}{\sigma_a} \right)^2 \quad \text{(A2)}$$

with respect to the fit parameters p, where $f(x_i; p)$ is the corresponding fit function with parameters p (functions of the amplitudes, energies and matrix elements), y is the data, and the (estimated) covariance matrix σ^y is

$$\sigma^y_{ij} = \frac{\overline{f(x_i; p)f(x_j; p)} - \overline{f(x_i; p)}\,\overline{f(x_j; p)}}{N_s(N_s - 1)}. \quad \text{(A3)}$$

The prior distribution for the parameter p_a in the fit function $f(x_i; p)$ is the normal distribution $\mathcal{N}(p_a^{\text{prior}}, \sigma_a)$. Therefore, the function to be minimized is $\chi^2_{\text{aug}} = \chi^2 + \chi^2_{\text{prior}}$ [34–36].

The covariance matrix σ^y of the correlation function data is very large, so small eigenvalues of the covariance matrix are underestimated [48,69], causing problems when carrying out the inversion of σ^y in Eq. (A1) to find χ^2. This is overcome by using a singular-value decomposition (SVD) cut; any eigenvalue of the covariance matrix smaller than some proportion c of the biggest eigenvalue λ_{max} is replaced by $c\lambda_{\text{max}}$. By carrying out this procedure, the covariance matrix becomes less singular. These eigenvalue replacements will only inflate our final errors; hence, this strategy is conservative. The $\chi^2/\text{d.o.f.}$ values are affected by the SVD cut, demonstrated in Appendix D of [48].

Priors for ground state energies, amplitudes and matrix elements ($V_{\text{nn},00}$) are motivated by plateaus in plots of effective quantities. For example, a straightforward effective energy can be constructed from a two-point correlation function as

$$aE_{\text{eff}} = -\log\left(\frac{C_{2\text{pt}}(t)}{C_{2\text{pt}}(t-1)} \right) \quad \text{(A4)}$$

and the effective simulation amplitude

$$a_{\text{eff}} = \sqrt{C_{2\text{pt}}(t)e^{aE_{\text{eff}}(t)}}. \quad \text{(A5)}$$

Priors associated with the oscillating and excited states are informed by our previous experiences. From expectations of QCD, the energy splittings between excited states are taken as $a\Lambda_{\text{QCD}} \times 2(1)$ where Λ_{QCD} is taken to be 500 MeV. The prior for the energy of the lowest-lying oscillating state is given a prior twice as wide as the prior for the energy of the nonoscillating ground state. The log of the amplitudes for the oscillating states and the remaining nonoscillating states are given priors of $-2.3(4.6)$. Finally, $V_{\text{nn},ij}$ for $i.j$ other than $i = j = 0$ are given priors of $0(1)$ for the case of insertions of the scalar density and temporal vector current, and $0.0(5)$ for the tensor current insertion.

A variety of different fits are carried out with different SVD cuts, numbers of exponentials, and trims of correlator data at early and late times. Results from these fits are inspected in Appendix A 4. Insensitivity to these choices is observed, thus demonstrating stable and robust determination of the matrix elements. The SVD cuts considered for each lattice are based around the suggested cut given by the `svd_diagnosis` tool within the *corrfitter* package [33].

2. Energies and amplitudes

As described in Appendix A 1, plots of effective energies and amplitudes from Eqs. (A4) and (A5) are inspected to guide the selection of suitable priors for the nonoscillating ground states. The ground state energies from the fit are always within their prior distribution, and the error from the fit is always at least considerably smaller than the error on the prior.

For the purposes of demonstration, we consider the effective energies on set 1 (the fine lattice). Figure 18 shows how the effective energies for the H_s pseudoscalar meson plateau over the first 35 timeslices. The behavior is an oscillatory decay towards a plateau whose position is read off and used as the mean of the prior value accompanied by a broad error that comfortably accounts for any misreading of the plateau position. Similar behavior is observed for the other three sets in Table I. The size of the oscillatory behavior differs according to which two-point correlation function is being analyzed. The effective energy for the D_s pseudoscalar with interpolator $\gamma_5 \otimes \gamma_5$ in Fig. 19 shows almost no oscillatory contamination, whereas the effective energy for the D_s meson with taste $\gamma_5\gamma_0 \otimes \gamma_5\gamma_0$ in Fig. 20 fluctuates strongly between early timeslices; nevertheless, a plateau emerges at later timeslices, which indicates a suitable prior.

3. Vector current renormalization

For each heavy-quark mass, the renormalization factor Z_V is obtained at zero recoil using Eq. (6). Results are plotted in Fig. 21. The smallest uncertainties are observed on sets 1 and 2 (red and blue points), which have the best
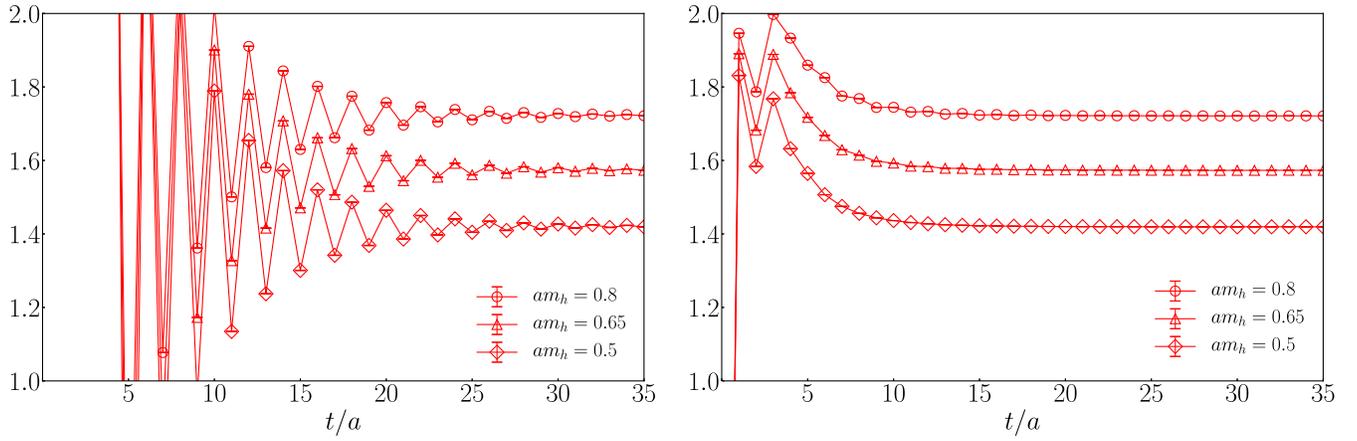
FIG. 18. Plots of effective energies for the pseudoscalar heavy-charm meson at each am_h value for set 1. The left plot shows the $\gamma_5 \gamma_t \otimes \gamma_5 \gamma_t$ meson. The right plot shows the $\gamma_5 \otimes \gamma_5$ meson.
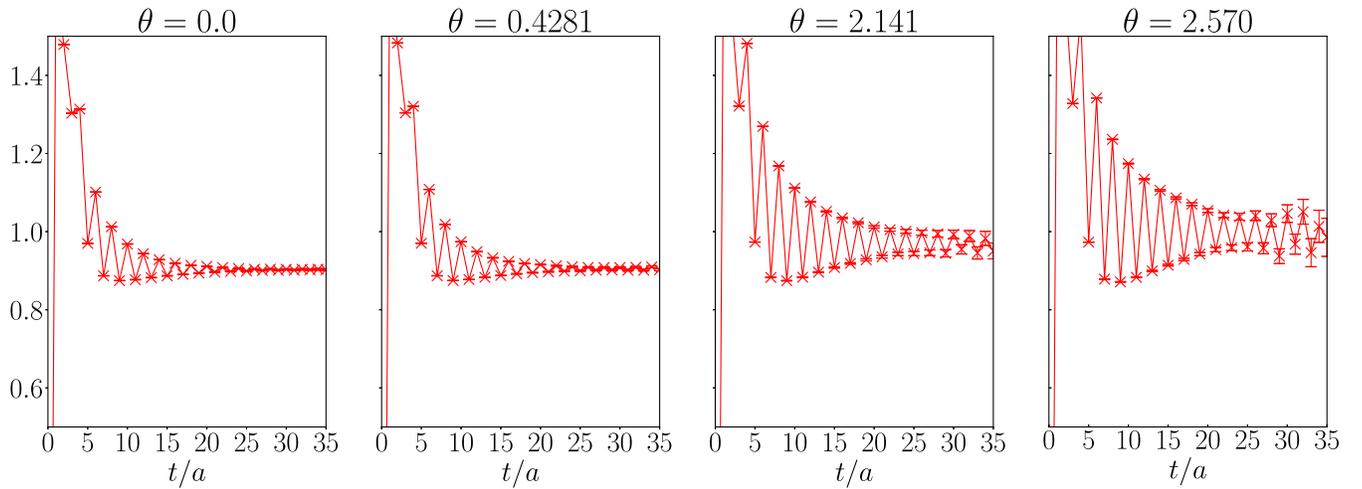
FIG. 19. Plots of effective energies for the D_s meson with taste $\gamma_5 \otimes \gamma_5$ at each twist in Table II for set 1.
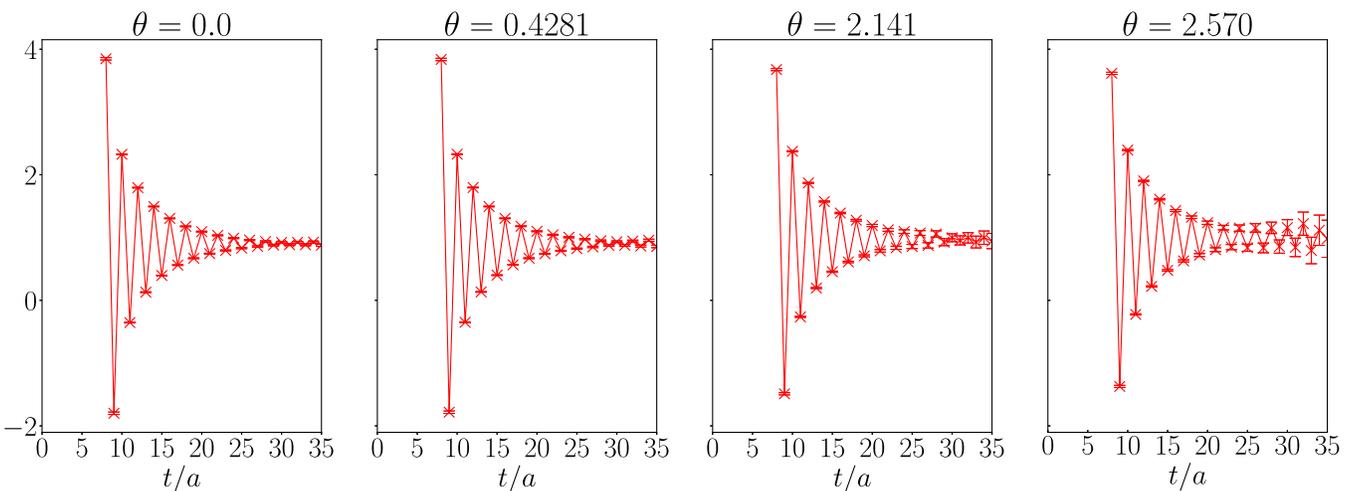
FIG. 20. Plots of effective energies for the D_s meson with taste $\gamma_5 \gamma_0 \otimes \gamma_5 \gamma_0$ at each twist in Table II for set 1.
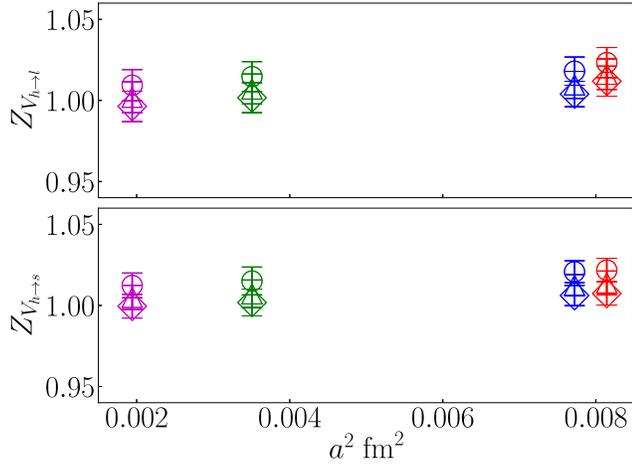
FIG. 21. Results for the local vector current renormalization factor Z_V obtained from Eq. (6) by the ratio of scalar density and temporal vector current matrix elements at zero recoil. The top and bottom plots show the results from the calculation of $B_c \rightarrow D_l$ and $B_c \rightarrow D_s$. The different colors and shapes of markers relate to sets and am_h values as described in Fig. 2.

statistics. The differences between the top ($B_c \rightarrow D_l$) and bottom ($B_c \rightarrow D_s$) plots are very small. This is expected since the Z_V values in the two plots differ only by a discretization effect associated with the mass of the two daughter quarks, strange and light, which are both small. The figure suggests a mild discretization effect associated with the bare heavy quark mass am_h, though the values are comparable across the four sets. The central values for Z_V with $am_h = 0.8$ are positioned above the other two values for am_h for each set. Discretization errors associated with am_h are taken into consideration when fitting the form factor data obtained on the lattices.

4. Stability of correlation function fits

We are required to make many choices when fitting the correlation functions to the forms given in Eqs. (10) and (13). However, we demonstrate in this section that the fit results for the sought-after ground state quantities are insensitive to the particular strategy of any given fit. In fact, we explore many different choices to assess robustness. For the purposes of demonstration, Fig. 22 shows a selection of matrix elements plotted against I, enumerating different fits, which we now describe. By inspecting this plot, we can identify a region in the space of fitting strategies where the fit results are stable and reasonable.

In Table IX, we tabulate the regimes for each set used in our final determination of the physical-continuum form factors. These fits are chosen from a variety of fits that, as explained in Sec. II E, use different SVD cuts, numbers of exponentials, and trims of the correlator data. To demonstrate the robustness of the correlation function fits used to extract the form factor data, we show that the fits are stable

and are selected among regions in parameter space where the matrix elements are insensitive to these choices of fitting regime. In Fig. 22, as an example, we display results for the $V_{nn,00}$ parameter associated with the scalar density at zero recoil for $am_h = 0.65$ on each of the four sets in Table I (similar behavior is found for the other currents, momenta and heavy quark masses). We plot $V_{nn,00}$ against an index I, which enumerates the fit. We define I as

$$I = n_i + 3s_i + 15t_i^{3pt} + 75t_i^{2pt} \qquad (A6)$$

where $n_i = 0$, 1, 2 indexes the choice of the number of exponentials $N_n + N_o \in \{4, 5, 6\}$, and $s_i = 0$, 1, 2, 3 indexes the choice of SVD cut in either $\{0.0075, 0.005, 0.0025, 0.001\}$ for sets 1 and 2, or the set $\{0.01, 0.0075, 0.005, 0.0025\}$ for sets 3 and 4. These ranges of SVD cut cover the recommendation from the svd_diagnosis tool within the *corrfitter* package [33]. We investigate the effect of trimming the correlator data: $0 \leq t_i^{2pt}$, $t_i^{3pt} \leq 3$ indexes the choice of t_{min}^{2pt}/a and t_{min}^{3pt}/a in $\{2, 4, 6, 8\}$ for sets 1 and 2, in $\{6, 8, 10, 12\}$ for set 3, and in $\{8, 10, 12, 14\}$ for set 4. We are guided by the expectation that we should trim according to some fixed distance in physical units away from the interpolator. Hence, we generally trim more data points for finer lattices. Note that t_{min}^{2pt} is the slowest running parameter. To aid the reader's understanding of the organization of the fits in Fig. 22, we separate fits with different values of t_{min}^{2pt}/a with black dashed vertical lines.

Considering figures such as Fig. 22 for all matrix elements helps us to identify choices of parameters where the fit is stable while also ensuring that we avoid unnecessarily bloated fit models with more exponentials than required. The fit takes longer to complete for more exponentials; hence, a judicious selection of N_n and N_o allows us to feasibly explore, in reasonable computing time, the parameter landscape in other directions. Nevertheless, a variety of fits with $N_n + N_o = 7$, 8 and greater have also been carried out to ensure that the convergence demonstrated in Fig. 22 is maintained for more exponentials. Indeed, similar extractions of the ground state quantities are obtained by these fits. For the purposes of fitting form factors, it suffices to use fits with $N_n + N_o = 7$ or 8 on sets 1 and 2, and $N_n + N_o = 5$ or 6 on sets 3 and 4. In summary, each plot shows results from 192 different fits ($0 \leq I \leq 191$). The parameters used for our final fits are shown by the bold entries in Table IX, and the plots demonstrate that these choices lie within regions of parameter space that admit stable fit results.

First, we address the dependence on the number of exponentials. In Fig. 22, we show fits for $N_n + N_o \in \{4, 5, 6\}$ with $N_n - N_o = 0$ for $N_n + N_o$ even, and $N_n - N_o = 1$ for $N_n + N_o$ odd. The fits with $N_n + N_o = 4$ show some variation as the other parameters are varied, particularly for smaller t_{min}^{2pt}/a and smaller SVD cuts. In contrast, fits with $N_n + N_o = 5$ and $N_n + N_o = 6$ are in good
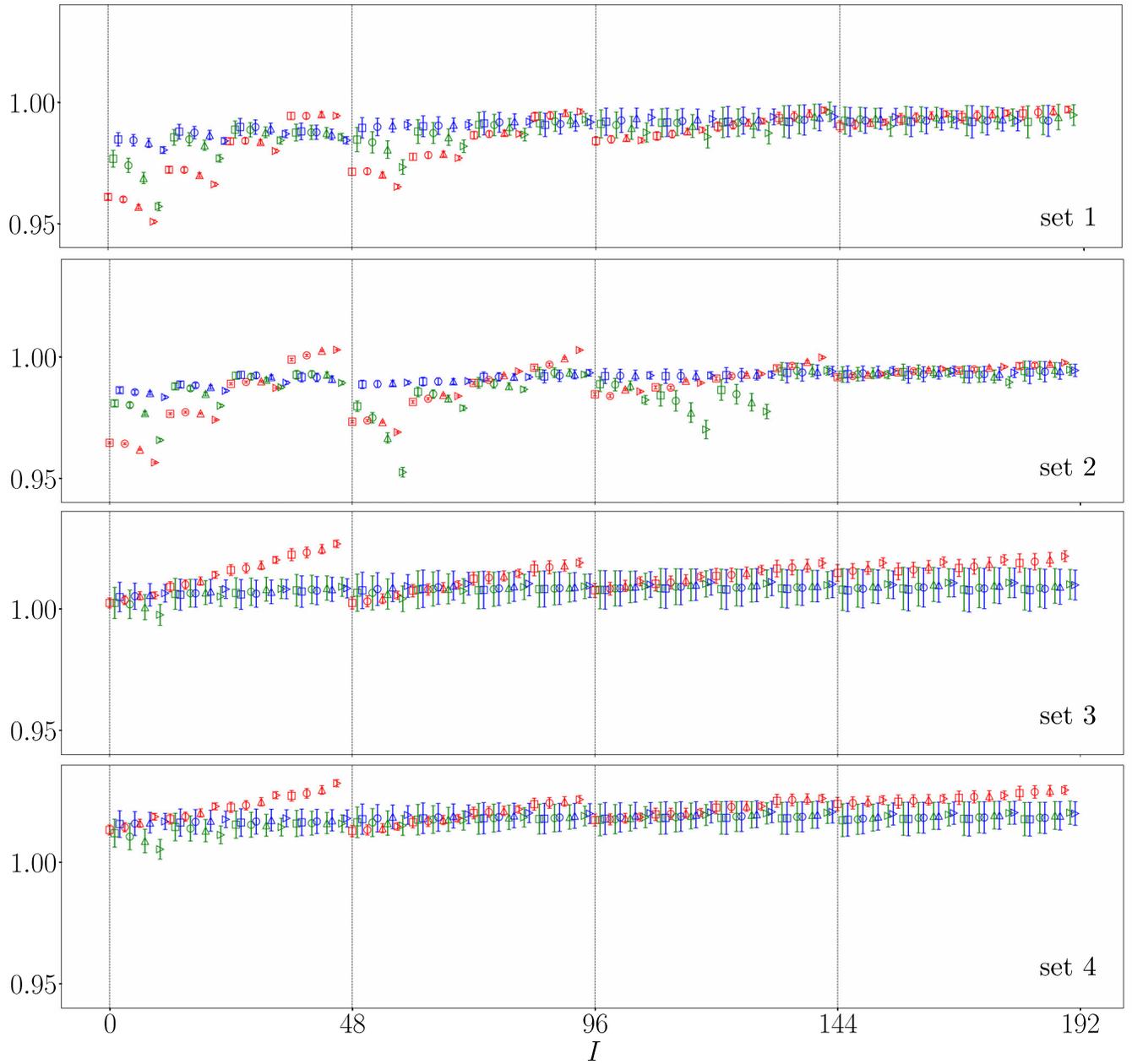
FIG. 22. Parameter $V_{nn,00}$ from Eq. (13) corresponding to the $H_c \to D_s$ three-point correlator at zero recoil with $am_h = 0.65$ plotted against the fit index I [defined in Eq. (A6)]. From top to bottom, results on sets 1, 2, 3 and 4 (see Table I) are presented respectively. Red, green and blue points indicate that the fit used $N_n + N_o = 4, 5, 6$ exponentials respectively (see Eqs. (10) and (13)). The different marker styles reflect the SVD cut chosen: squares, circles, triangles, right and left pointing triangles correspond to SVD cuts of 0.001, 0.025, 0.05, 0.075 and 0.01 respectively. The scale of the y axis is shared by the four plots. We scrutinise the form factors associated with correlator fits detailed in Table IX.

agreement with each other for most choices of SVD cut and larger correlator function trims, and there are clear regions where $V_{nn,00}$ appear stable.

Addressing the different extents that correlation function data have been trimmed, the fit results show some mild instability for $t_{min}^{2pt}/a = 2$ where the correlation function data to be fit contain the most excited state contamination. This instability is expected to be better resolved by

introducing more exponentials that can absorb more contributions from higher energy states and short-distance effects. For example, fits with $t_{min}^{2pt}/a > 2$ appear more stable than those for $t_{min}^{2pt}/a = 2$.

Finally, we discuss the behavior of the fit results as the SVD cut is varied, denoted by different marker styles in Fig. 22. It is consistently apparent throughout the fits on each set that increasing the SVD cut has the effect of

TABLE IX. Input parameters (see text for definition) to the fits of correlation functions for the heavy-HISQ calculation together with fits including variations of the SVD cut, t_{min}^{2pt}/a, t_{min}^{3pt}/a and N. Bold entries indicate those fits used to obtain the final results. Other values are used in tests of the stability of our form factor fits to be discussed in Appendix B 3.

Set	$B_c \to D_l$				$B_c \to D_s$			
	SVD	t_{min}^{2pt}/a	t_{min}^{3pt}/a	N	SVD	t_{min}^{2pt}/a	t_{min}^{3pt}/a	N
1	**0.005**	**4**	**4**	**8**	**0.005**	**6**	**4**	**7**
	0.0025	8	8	8	0.0025	6	2	7
2	**0.0025**	**4**	**6**	**8**	**0.005**	**6**	**6**	**7**
	0.005	4	8	8	0.0025	8	6	8
3	**0.005**	**8**	**8**	**6**	**0.005**	**10**	**10**	**6**
	0.0075	10	10	5	0.005	10	12	5
4	**0.0075**	**10**	**12**	**6**	**0.0075**	**12**	**12**	**6**
	0.0075	10	10	5	0.0075	10	14	6

increasing the error on the value obtained for the V_{nn} parameter. The matrix elements extracted are consistent with each other as the SVD cut is increased, so it appears from these plots that using too large a SVD cut is too conservative. Decreasing the SVD cut substantially below the recommended cut taken from the svd_diagnosis tool within the *corrfitter* package [33] gives unstable and unreliable results. Hence, we do not deviate far from this recommended cut. On the finer lattices, sets 3 and 4, fits with a SVD cut of 0.001 are frequently in tension with the other fits. While this may be an appropriate SVD cut for some fits on sets 1 and 2, the same is not true on sets 3 and 4. This is unsurprising since sets 3 and 4 have poorer statistics than sets 1 and 2. Fits on sets 3 and 4 benefit from a larger SVD cut. Indeed, in Table IX, we show that we take fits with SVD cuts of no smaller than 0.005 for sets 3 and 4. SVD cuts for sets 1 and 2 are chosen among 0.0025 and 0.005. Obtaining higher statistics on sets 3 and 4 would enable a smaller SVD cut to be taken, thus achieving a smaller error on the extracted matrix elements.

In conclusion, based on our exploration of different fits, it is clear that fitting with larger trims of the correlation function data is warranted for the finer lattices, reflected by our choice of fits in Table IX. The finer lattices also require fewer exponentials and slightly larger SVD cuts than the fine and fine-physical sets.

APPENDIX B: FORM FACTOR FITTING ANALYSIS

1. Fit results

In Figs. 23 and 24, we show our form factor data alongside the fit functions tuned to the physical-continuum point. Note that the q^2 corresponding to zero recoil, $q_{max}^2 = (M_{H_c} - M_{D_{l(s)}})^2$, varies as a function of the heavy quark mass. Hence, the spread over q^2 of the form factor data for larger am_h is greater than for smaller am_h on each set. See Fig. 2 for the q^2 we access as a proportion of q_{max}^2 on each set and heavy quark mass am_h.

Errors on the data for f_+ near zero recoil are large, and we exclude points with errors in excess of 25% from the fit. These large errors are a result of the kinematic factors associated with determining f_+ from the temporal vector current matrix elements [see Eq. (8)]. Further discussion can be found in Sec. II C of [7] and Sec. IV B here.

Figures 25 and 26 show the same data and fit after multiplying by the pole factor $P(q^2)$ [see Eq. (16)]. The fit function shown in Eq. (16) is the polynomial in z that gives
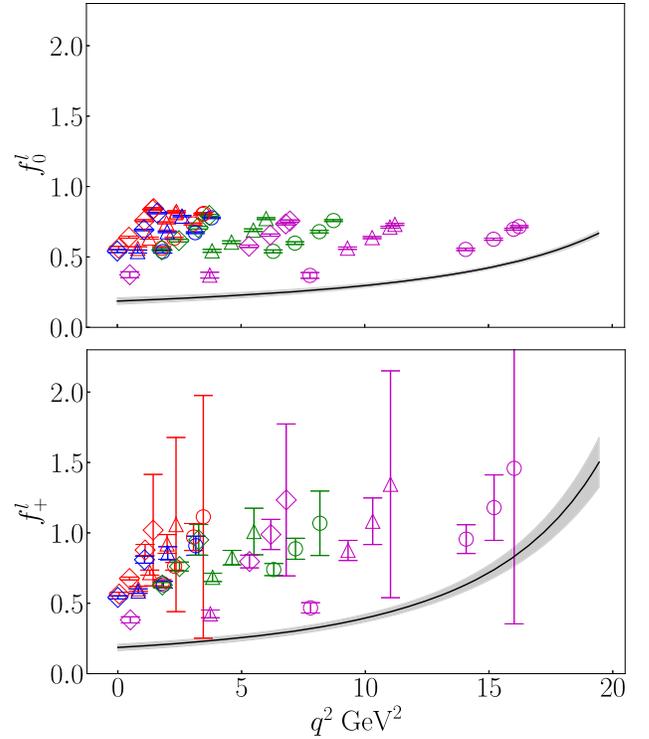
FIG. 23. Data and fit for the form factors $f_{0,+}^l$. The scale of the y-axis is the same as for Fig. 24. The different colours and shapes of markers relate to sets and am_h values as described in Fig. 2.
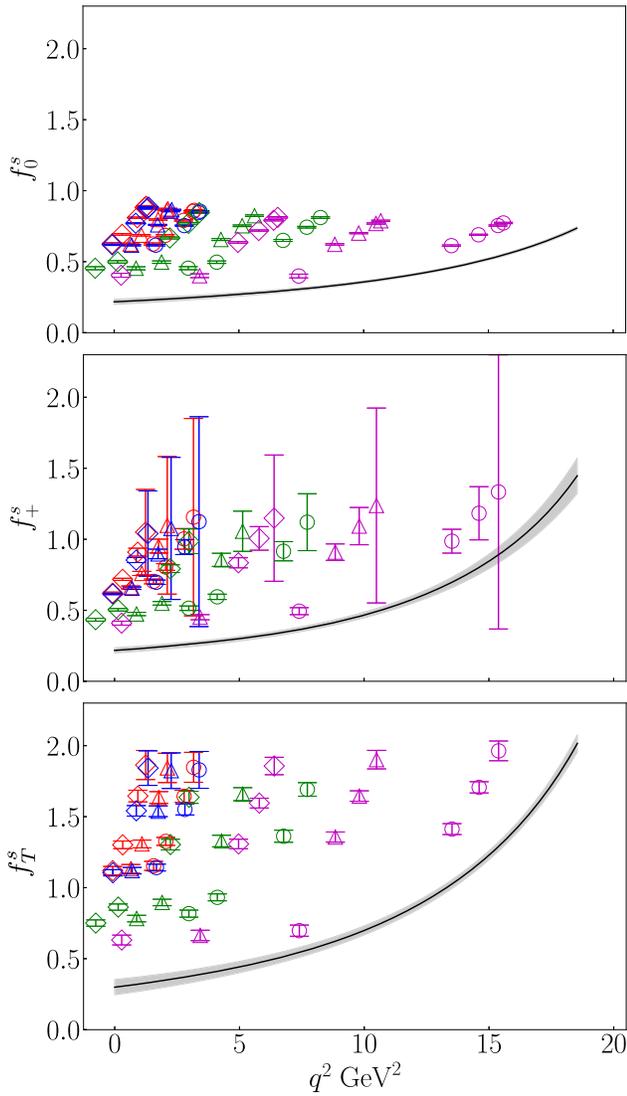
FIG. 24. Data and fit for the form factors $f_{0,+,T}^s$. The scale of the y-axis is shared with Fig. 23.

FIG. 25. Data and fit for the form factors $f_{0,+}^l$ multiplied by the pole factor $P(q^2)$ [see Eq. (16)]. The fit band is the polynomial $\sum_n c^{(n)} (-z)^n$ [coefficients $c^{(n)}$ are defined in Eq. (C2)].

the residual momentum dependence of the form factors not accounted for by the pole factor $P(q^2)^{-1}$. Note that the y axis is smaller in Figs. 25 and 26 than for Figs. 23 and 24 since most of the q^2 dependence of the form factors has been removed on multiplying by the pole factor $P(q^2)$. The polynomial for f_0 appears linear in z-space to a good approximation. For $f_{+,T}$, the fit curves show a small amount of curvature. We compare fits with $N_n = 3$ and 4 in Appendix B 3 to ensure that our truncation of the z-expansion is appropriate.

As is standard with heavy-HISQ analyses of decays of a valence b quark, the q^2 dependence of the form factors is inferred from data on multiple lattices, which each have a different range of q^2 since $q_{\max}^2$ varies with am_h. This can make the plots shown in Figs. 23–26 difficult to interpret

since there are several different extrapolations taking place simultaneously to reach the fit curve in the continuum limit with physical quark masses. Considering just the data at zero recoil can provide a clearer understanding of how the fit curves shown in the figures relate to the lattice data for the form factors. Figure 27 shows, for both the cases $B_c \to D_l$ and $B_c \to D_s$, data for f_0 at zero recoil plotted against M_{H_c} alongside the fit function tuned to the continuum limit with physical light, strange and charm quark masses. This figure shows how the dependence on the heavy quark mass is resolved by the factors $\Omega^{(n)} (\Lambda/M_{H_{l(s)}})^r$ in Eq. (16). For the purposes of presenting the fit as a continuous function of the M_{H_c}, we approximate the heavy-light and heavy-strange pseudoscalar mass as $M_{H_q} \approx M_{H_c} - (M_{B_c} - M_{B_q})$ where $q = l$ or s. The lattice data follow the curve closely. The error band is most narrow at around 4 GeV, and the error flares slightly as M_{H_c} approaches M_{B_c}.

2. Imposition of the kinematic constraints

The form factors must obey $f_0(0) = f_+(0)$ in the continuum limit for all masses of the heavy-charm pseudoscalar meson (see Sec. II F 2). Since we take $t_0 = 0$ in Eq. (15), $z = 0$ at $q^2 = 0$. Hence, the kinematic constraint
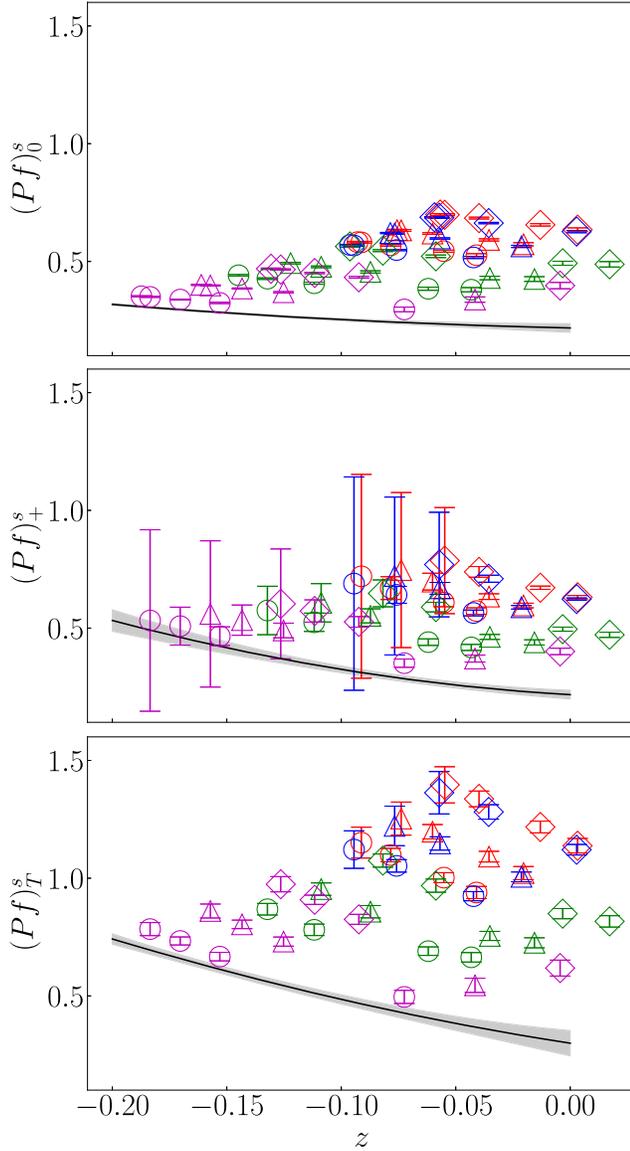
FIG. 26. Data and fit for the form factors $f^s_{0,+,T}$ multiplied by the pole factor $P(q^2)$] see Eq. (16). The fit band is the polynomial $\sum_n c^{(n)}(-z)^n$ [coefficients $c^{(n)}$ are defined in Eq. (C2)].

can be straightforwardly applied to our fit: we insist that $(A_0)^{(0r00)} = (A_+)^{(0r00)}$ for all r and $\rho^{(0)}_0 = \rho^{(0)}_+$ [see Eq. (16)] by setting a narrow prior on their differences. Table X compares the errors at the q^2 extremes from fitting with and without these parameter constraints. We also compare integrated quantities. The two fits are in good agreement. Uncertainties are reduced very slightly when fitting with the kinematics constraint. The form factors $f^l_{0,+}$ at $q^2 = 0$ see the most benefit.

3. Fit variations

In Table IX, we describe two different fits of correlation functions on each set and fit the form factors to each
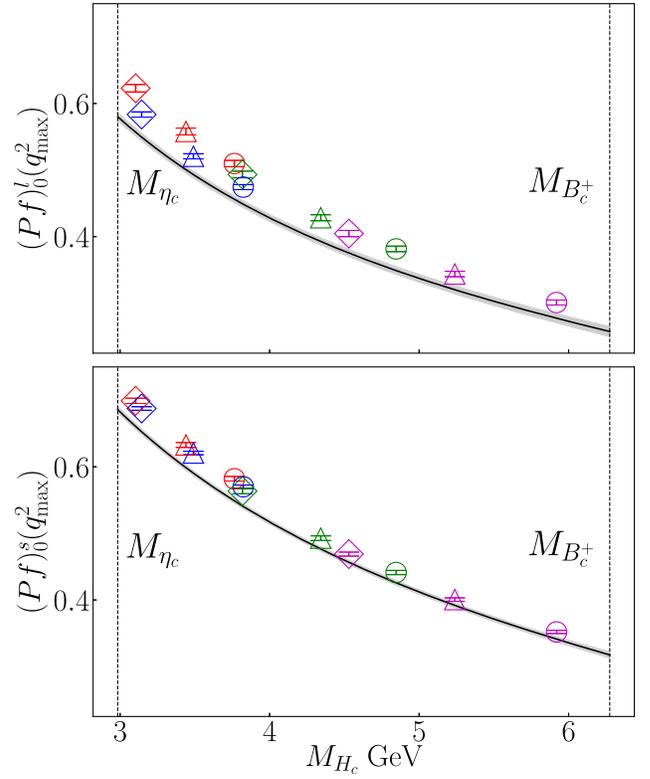
FIG. 27. Data and fit for the form factor f_0 multiplied by the pole factor [see Eq. (16)] plotted at zero recoil as a continuous function of M_{H_c}. The vertical dotted lines show the masses of the H_c meson for the cases in which the heavy quark coincides with the charm and bottom quarks.

TABLE X. We compare fits with and without imposition of the kinematic constraint (KC) $f_0(0) = f_+(0)$. Form factors are shown at $q^2 = 0$ and maximum q^2. We also present integrated values where we find the variation between the two fits to be especially small. The three uncertainties on the branching fractions are from the lattice, the lifetime of the B_c meson, and V_{ub}, respectively.

	Final	Without KC
$f^l_0(0)$	0.186(23)	0.191(27)
$f^l_+(0)$	…	0.158(34)
$f^l_0(q^2_{max})$	0.668(20)	0.669(20)
$f^l_+(q^2_{max})$	1.50(18)	1.48(17)
$\mathcal{B}(B^+_c \to D^0 e^+ \nu_e) \times 10^5$	3.37(48)(8)(42)	3.17(51)(8)(40)
$\mathcal{B}(B^+_c \to D^0 \tau^+ \nu_\tau) \times 10^5$	2.29(23)(6)(29)	2.29(23)(6)(29)
$f^s_0(0)$	0.217(18)	0.224(19)
$f^s_+(0)$	…	0.192(23)
$f^s_0(q^2_{max})$	0.736(11)	0.736(11)
$f^s_+(q^2_{max})$	1.45(12)	1.44(12)
$\mathcal{B}(B^+_c \to D^+_s e^+ e^-) \times 10^7$	1.00(11)	0.95(11)
$\mathcal{B}(B^+_c \to D^+_s \tau^+ \tau^-) \times 10^7$	0.246(18)	0.246(18)
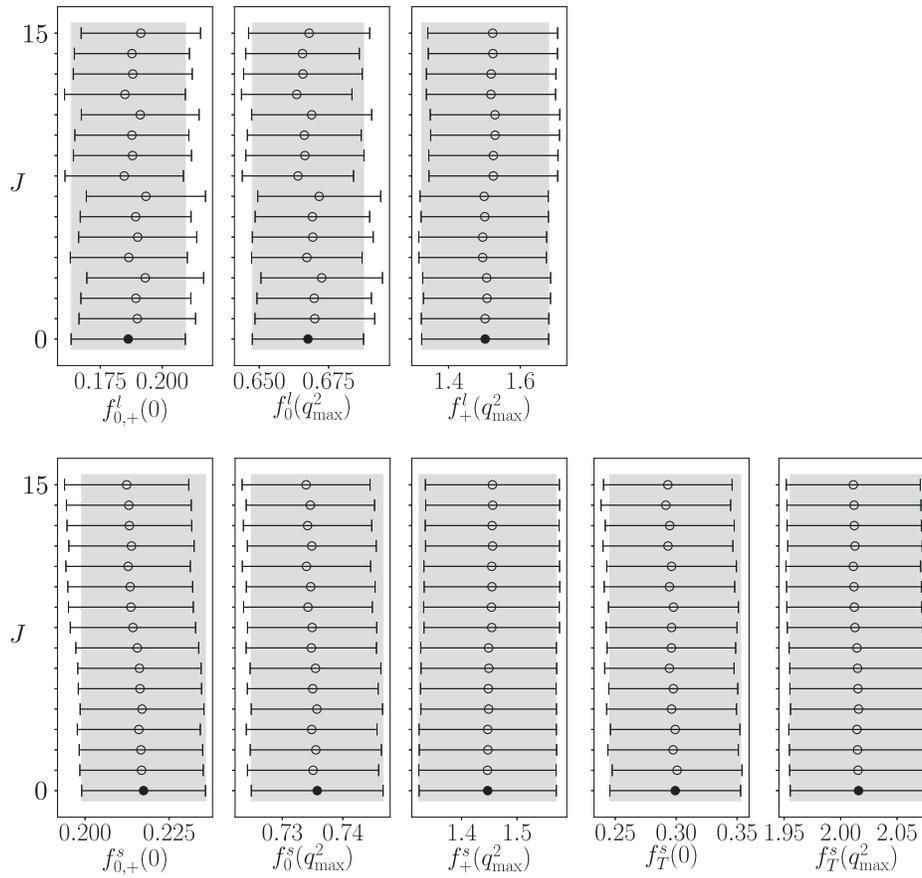
FIG. 28.　For each of the 16 different correlator fits indexed by J [see Eq. (B1)], we show the fitted values of the physical-continuum form factors for $B_c \rightarrow D_l$ (top) and $B_c \rightarrow D_s$ (bottom) evaluated at maximum q^2 and $q^2 = 0$. These plots show results from all possible combinations of the correlation function fits described in Table IX and demonstrate the stability of our results under these changes. The filled black points show the results from our final fit.

different combination, resulting in 16 different fits of the form factors. In Fig. 28, we show the physical-continuum form factors evaluated at $q^2 = 0$ and $q_{\max}^2$ from each of the fits. The fits are indexed by J where

$$J = \sum_{j=1}^{4} 2^{j-1} n_j \qquad (B1)$$

where $n_j \in \{0, 1\}$ indexes each of the two fits on set j given in Table IX. For example, the fit labeled by $J = 0$ uses correlation function fit results corresponding to all the bold entries in Table IX. The figure shows that the form factors are insensitive to the particular choice of correlator fits. The fit $J = 0$ yields form factors very similar to the 15 alternative fits with $J > 0$. All central values lie within the 1-σ error band of those parameters corresponding to the $J = 0$ fit from which our final results for the form factors are derived. We conclude that the form factor fits are robust and stable as the choices of correlation function fits are varied.

Next, we consider other variations of form factor fits. In Fig. 29, we show results from a variety of different fits which we now describe. The fit variations are labeled on the y axis. Our final fit, results from which we report in Sec. III, is labeled "final."

Beginning at the top of the plot for $f_{0,+}^l$, we consider removing the chiral log by setting $\mathcal{L} = 1$. The fit labeled "hard pion chiral PT" uses $\mathcal{L} = 1 + \zeta^{(0)} x_\pi \log x_\pi$ instead of the $\mathcal{L}$ given in Eq. (18). Similar fit results are achieved with these fit variations indicating that, with the current status of errors, the dependence on the light quark mass can be absorbed into the analytic terms in the $\mathcal{N}_{\mathrm{mis}}^{(n)}$ factor in the fit form at Eq. (16).

Next, we consider fits varying $N_{n,r,j,k}$ in the fit form at Eq. (16). Doing so allows us to investigate the impact of truncating our fit form. Varying N_n tests the truncation $N_n = 3$ of the z series for $P(q^2) f(q^2)$. Form factor values and errors at both $q^2 = 0$ and zero recoil change very little between fits with $N_n = 3, 4$. We use $N_n = 3$ in our final results. Similarly, increasing $N_{r,j,k}$ yields consistent fit results.
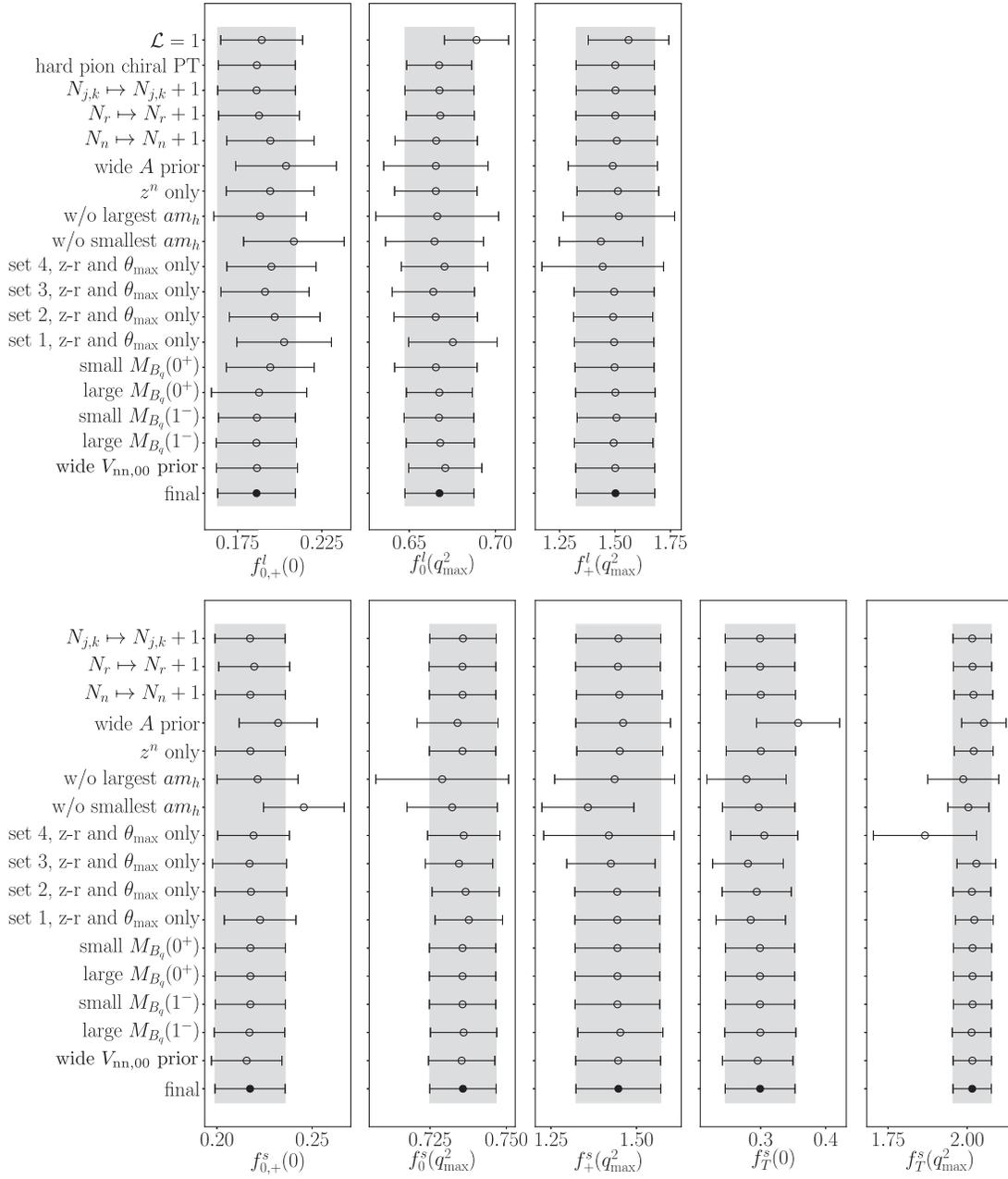
FIG. 29. For each of the different form factor fits described in Appendix B 3, we show the physical-continuum form factors for $B_c \to D_l$ (top) and $B_c \to D_s$ (bottom) evaluated at maximum q^2 and $q^2 = 0$. The filled black points show the results from our final fit.

Results from increasing prior widths of parameters $A^{(nrjk)}$ and $\rho^{(n)}$ are shown next. The fit results are in agreement with our normal priors. Recall in Sec. III A that we perform an empirical Bayes analysis to check that our priors are appropriate.

Fits where the z^{N_n+1} terms are removed are shown. It appears as though these terms make very little difference to the form factors.

We then consider fitting with different subsets of the data. First, we consider fitting without the smallest and largest am_h values on all sets. Next, we remove certain

twists on the four different sets. Fitting with these smaller data sets gives form factors consistent with our final results. It is often the case that fitting with these reduced data sets gives errors larger than those observed when fitting with all of the data.

We also check that the fits are insensitive to the value given for M_{res} in $P(q^2)$ by perturbing the pole mass. In Sec. II F 3, we described how we estimate the masses of the heavy-strange (light) vector and scalar mesons used in the pole factor $P(q^2)$. With the pseudoscalar meson mass fixed, the splitting between the pseudoscalar and vector mesons is

changed by $\pm 50\%$, and similarly for the splitting of the pseudoscalar and scalar mesons. The agreement of the fits here suggests that the approximations made in Sec. II F 3 are appropriate. Finally, we show a fit that uses correlation functions in which the priors for $V_{nn,00}$ of each insertion are 25% wider.

Good agreement is observed between the fits shown in Fig. 29. Hence, we conclude that our fit of the form factors is robust.

APPENDIX C: RECONSTRUCTING THE FORM FACTORS

We now provide instructions for reconstructing our form factors in the continuum limit with physical quark masses. For the convenience of the reader, we have provided the script `construct_ffs.py` which constructs our form factors [10].

The form factors in the continuum limit ($a \to 0$) and the limit of physical masses [$\delta m = 0$ in Eq. (21)] are shown in Fig. 4. In these limits, the fit form collapses to the physical-continuum parametrization

$$f(q^2) = P(q^2)^{-1} \sum_{n=0}^{N_n} c^{(n)} \hat{z}^{(n,N_n)}. \tag{C1}$$

The values for the pole factors $P(q^2) = 1 - q^2/M_{\text{res}}^2$ in the case $m_h < m_b$ are discussed in Sec. II F 3. For $m_h = m_b$, we use the M_{res} values given in Table V. Recall that we define $\hat{z}^{(n,N_n)}$ in Eq. (17), and we take $t_0 = 0$ in Eq. (15). In the limit of vanishing lattice spacing and physical quark masses, the coefficients $c^{(n)}$ of the $\hat{z}^{(n,N_n)}$-polynomial $P(q^2)f(q^2)$ are given by

$$c^{(n)} = \mathcal{L} \sum_{r=0}^{N_r} A^{(nr00)} \Omega^{(n)} \left(\frac{\Lambda}{M_{H_{l(s)}}} \right)^r. \tag{C2}$$

Here, the factor $\mathcal{L}$ is given in Eq. (18), and we use the physical ratio m_l/m_s given in Eq. (23) to evaluate $x_\pi = m_l/5.63 m_s^{\text{tuned}}$. The coefficients ζ are determined by the fit. Also, the factors $\Omega^{(n)}$ given in Eq. (19) are evaluated for $M_{H_{l(s)}} = M_{B_{l(s)}}$.

TABLE XI. Values we take for various different meson masses. To reconstruct our form factors, these masses should be used in conjunction with the coefficients $c_{0,+,T}^{(n)}$ in the files `cn_BcDl.py` and `cn_BcDs.py` via Eq. (C1). The bottom four rows give the masses used in the pole factor $P(q^2)$, and the middle three rows are used to construct t_+ which is needed to transform q^2 into z via Eq. (15). The top three rows allow $q_{\text{max}}^2 = t_-$ to be found. These masses are featured in the script `construct_ffs.py`, which we provide.

Meson (J^P)	Mass GeV
$B_c(0^-)$	6.2749 [28]
$D(0^-)$	1.8648 [28]
$D_s(0^-)$	1.9690 [28]
$B(0^-)$	5.27964 [28]
$\pi(0^-)$	0.134977 [28]
$K(0^-)$	0.497611 [28]
$B(1^-)$	5.324 [28]
$B(0^+)$	5.627 [47]
$B_s(1^-)$	5.4158 [28]
$B_s(0^+)$	5.711 [46]

We now give values for the parameters needed to reconstruct the form factors using the form in Eq. (C1). First, we take $N_n = 3$ and $N_r = 2$. For $B_c \to D_l$ and $B_c \to D_s$, coefficients $c^{(n)}$ are given in the files `cn_BcDl.py` and `cn_BcDs.py` [10].

Table XI gives all meson masses required to construct the form factors. For $B_c \to D_l$, we use $t_- = (M_{B_c(0^-)} - M_{D(0^-)})^2$ and $t_+ = (M_{B(0^-)} + M_{\pi(0^-)})^2$. For $B_c \to D_s$, we use $t_- = (M_{B_c(0^-)} - M_{D_s(0^-)})^2$ and $t_+ = (M_{B(0^-)} + M_{K(0^-)})^2$. Recall that the pole factor is given by $P(q^2) = 1 - q^2/M_{\text{res}}^2$, where for M_{res}, we take the masses of the mesons $B(0^+)$, $B(1^-)$, $B_s(0^+)$ and $B_s(1^-)$ for f_0^l, f_+^l, f_0^s and $f_{+,T}^s$, respectively. The masses of the pseudoscalar and vector mesons are obtained from PDG [28]. Estimates for the masses of the scalar mesons are obtained from [46,47], though precise values are not necessary for our calculation. We do not include an error on these values. The reader should use these masses to exactly replicate the form factors shown in Fig. 4.

[1] B. Khanji *et al.* (LHCb Collaboration), *Proceedings of the Implications of LHCb Measurements and Future Prospects* (2020).

[2] Y. S. Amhis *et al.* (HFLAV Collaboration), Eur. Phys. J. C **81**, 226 (2021).

[3] J. Harrison, C. T. Davies, and A. Lytle (HPQCD Collaboration), Phys. Rev. D **102**, 094518 (2020).

[4] E. Follana, Q. Mason, C. Davies, K. Hornbostel, G. P. Lepage, J. Shigemitsu, H. Trottier, and K. Wong (HPQCD and UKQCD Collaborations), Phys. Rev. D **75**, 054502 (2007).

[5] E. McLean, C. T. H. Davies, A. T. Lytle, and J. Koponen, Phys. Rev. D **99**, 114512 (2019).

[6] E. McLean, C. T. H. Davies, J. Koponen, and A. T. Lytle, Phys. Rev. D **101**, 074513 (2020).

[7] L. J. Cooper, C. T. H. Davies, J. Harrison, J. Komijani, and M. Wingate (HPQCD Collaboration), Phys. Rev. D **102,** 014513 (2020); **103,** 099901(E) (2021).

[8] W. Parrott, C. Bouchard, C. Davies, and D. Hatton, Phys. Rev. D **103,** 094506 (2021).

[9] J. Harrison and C. T. H. Davies (LATTICE-HPQCD Collaboration), arXiv:2105.11433.

[10] See Supplemental Material at http://link.aps.org/supplemental/10.1103/PhysRevD.105.014503 for results from fitting the correlations functions and our final form factors.

[11] A. Sirlin, Nucl. Phys. **B196,** 83 (1982).

[12] C. Bouchard, G. Lepage, C. Monahan, H. Na, and J. Shigemitsu (HPQCD Collaboration), Phys. Rev. D **88,** 054509 (2013); **88,** 079901(E) (2013).

[13] A. J. Buras, J. Girrbach-Noe, C. Niehoff, and D. M. Straub, J. High Energy Phys. 02 (2015) 184.

[14] W. Altmannshofer, A. J. Buras, D. M. Straub, and M. Wick, J. High Energy Phys. 04 (2009) 022.

[15] A. Bazavov et al. (MILC Collaboration), Phys. Rev. D **82,** 074501 (2010).

[16] A. Bazavov et al. (MILC Collaboration), Phys. Rev. D **87,** 054505 (2013).

[17] A. Bazavov et al. (MILC Collaboration), Phys. Rev. D **93,** 094510 (2016).

[18] A. Hart, G. M. von Hippel, and R. R. Horgan (HPQCD Collaboration), Phys. Rev. D **79,** 074008 (2009).

[19] S. Borsanyi et al., J. High Energy Phys. 09 (2012) 010.

[20] R. J. Dowdall, C. T. H. Davies, G. P. Lepage, and C. McNeile, Phys. Rev. D **88,** 074504 (2013).

[21] B. Chakraborty, C. T. H. Davies, P. G. de Oliviera, J. Koponen, G. P. Lepage, and R. S. Van de Water, Phys. Rev. D **96,** 034516 (2017).

[22] B. Chakraborty, C. T. H. Davies, B. Galloway, P. Knecht, J. Koponen, G. C. Donald, R. J. Dowdall, G. P. Lepage, and C. McNeile, Phys. Rev. D **91,** 054508 (2015).

[23] A. Bazavov et al. (Fermilab Lattice and MILC Collaborations), Phys. Rev. D **90,** 074509 (2014).

[24] A. Bazavov et al., Phys. Rev. D **98,** 074512 (2018).

[25] J. Koponen, A. C. Zimermmane-Santos, C. T. H. Davies, G. P. Lepage, and A. T. Lytle, Phys. Rev. D **96,** 054501 (2017).

[26] MILC Code Repository, https://github.com/milc-qcd.

[27] C. Bernard and D. Toussaint (MILC Collaboration), Phys. Rev. D **97,** 074502 (2018).

[28] M. Tanabashi et al. (Particle Data Group), Phys. Rev. D **98,** 030001 (2018).

[29] C. T. Sachrajda and G. Villadoro, Phys. Lett. B **609,** 73 (2005).

[30] D. Guadagnoli, F. Mescia, and S. Simula, Phys. Rev. D **73,** 114504 (2006).

[31] D. Hatton, C. T. H. Davies, G. P. Lepage, and A. T. Lytle (HPQCD Collaboration), Phys. Rev. D **100,** 114513 (2019).

[32] D. Hatton, C. T. H. Davies, G. P. Lepage, and A. T. Lytle (HPQCD Collaboration), Phys. Rev. D **102,** 094509 (2020).

[33] G. P. Lepage, Corrfitter Version 6.0.7 (github.com/gplepage/corrfitter).

[34] G. P. Lepage, B. Clark, C. T. H. Davies, K. Hornbostel, P. B. Mackenzie, C. Morningstar, and H. Trottier, Nucl. Phys. B, Proc. Suppl. **106,** 12 (2002).

[35] K. Hornbostel, G. P. Lepage, C. T. H. Davies, R. J. Dowdall, H. Na, and J. Shigemitsu, Phys. Rev. D **85,** 031504 (2012).

[36] C. M. Bouchard, G. P. Lepage, C. Monahan, H. Na, and J. Shigemitsu, Phys. Rev. D **90,** 054506 (2014).

[37] G. P. Lepage, lsqfit Version 11.1 (github.com/gplepage/lsqfit).

[38] C. G. Boyd and M. J. Savage, Phys. Rev. D **56,** 303 (1997).

[39] C. Bourrely, I. Caprini, and L. Lellouch, Phys. Rev. D **79,** 013008 (2009); **82,** 099902(E) (2010).

[40] B. Chakraborty, W. G. Parrott, C. Bouchard, C. T. H. Davies, J. Koponen, and G. P. Lepage, Phys. Rev. D **104,** 034505 (2021).

[41] J. Charles, A. Le Yaouanc, L. Oliver, O. Pene, and J. C. Raynal, Phys. Rev. D **60,** 014001 (1999).

[42] M. Tanabashi et al. (Particle Data Group), Phys. Rev. D **98,** 030001 (2018).

[43] D. Hatton, C. T. H. Davies, B. Galloway, J. Koponen, G. P. Lepage, and A. T. Lytle (HPQCD Collaboration), Phys. Rev. D **102,** 054511 (2020).

[44] A. F. Falk and M. Neubert, Phys. Rev. D **47,** 2982 (1993).

[45] H. Georgi, Phys. Lett. B **240,** 447 (1990).

[46] C. B. Lang, D. Mohler, S. Prelovsek, and R. M. Woloshyn, Phys. Lett. B **750,** 17 (2015).

[47] W. A. Bardeen, E. J. Eichten, and C. T. Hill, Phys. Rev. D **68,** 054024 (2003).

[48] R. J. Dowdall, C. T. H. Davies, R. R. Horgan, G. P. Lepage, C. J. Monahan, J. Shigemitsu, and M. Wingate, Phys. Rev. D **100,** 094508 (2019).

[49] V. Lubicz, L. Riggio, G. Salerno, S. Simula, and C. Tarantino (ETM Collaboration), Phys. Rev. D **96,** 054514 (2017); **99,** 099902(E) (2019); **100,** 079901(E) (2019).

[50] G. P. Lepage, gvar Version 9.22 (github.com/gplepage/gvar).

[51] P. A. Zyla et al. (Particle Data Group), Prog. Theor. Exp. Phys. **2020,** 083C01 (2020).

[52] R. Aaij et al. (LHCb Collaboration), Phys. Lett. B **742,** 29 (2015).

[53] E. E. Jenkins, M. E. Luke, A. V. Manohar, and M. J. Savage, Nucl. Phys. **B390,** 463 (1993).

[54] D. Leljak and B. Melic, J. High Energy Phys. 02 (2020) 171.

[55] D. Becirevic, N. Kosnik, F. Mescia, and E. Schneider, Phys. Rev. D **86,** 034034 (2012).

[56] A. Khodjamirian, T. Mannel, and Y. M. Wang, J. High Energy Phys. 02 (2013) 010.

[57] C. Hambrock, A. Khodjamirian, and A. Rusov, Phys. Rev. D **92,** 074020 (2015).

[58] J. Charles, A. Hocker, H. Lacker, S. Laplace, F. R. Le Diberder, J. Malcles, J. Ocariz, M. Pivk, and L. Roos (CKMfitter Group), Eur. Phys. J. C **41,** 1 (2005).

[59] A. T. Lytle, C. T. H. Davies, D. Hatton, G. P. Lepage, and C. Sturm (HPQCD Collaboration), Phys. Rev. D **98,** 014513 (2018).

[60] D. Hatton, C. T. H. Davies, J. Koponen, G. P. Lepage, and A. T. Lytle, Phys. Rev. D **103,** 114508 (2021).

[61] K. Melnikov and T. v. Ritbergen, Phys. Lett. B **482,** 99 (2000).

[62] M. Beneke and V. M. Braun, Nucl. Phys. **B426,** 301 (1994).

[63] R. Aaij *et al.* (LHCb Collaboration), J. High Energy Phys. 07 (2012) 133.

[64] D. Du, A. X. El-Khadra, S. Gottlieb, A. S. Kronfeld, J. Laiho, E. Lunghi, R. S. Van de Water, and R. Zhou, Phys. Rev. D **93**, 034005 (2016).

[65] P. Zyla *et al.* (Particle Data Group), Prog. Theor. Exp. Phys. **2020**, 083C01 (2020).

[66] C. Bobeth, G. Hiller, and G. Piranishvili, J. High Energy Phys. 12 (2007) 040.

[67] J. Brod, M. Gorbahn, and E. Stamou, Phys. Rev. D **83**, 034030 (2011).

[68] R. Aaij *et al.* (LHCb Collaboration), arXiv:1808.08865.

[69] C. Michael, Phys. Rev. D **49**, 2616 (1994).